A&A 552, A8 (2013)
DOI: 10.1051/0004-6361/201220551

Astronomy & Astrophysics

The *Herschel* Virgo Cluster Survey

XIII. Dust in early-type galaxies⋆,⋆⋆

S. di Serego Alighieri[1], S. Bianchi[1], C. Pappalardo[1], S. Zibetti[1], R. Auld[2], M. Baes[3], G. Bendo[4], E. Corbelli[1], J. I. Davies[2], T. Davis[5], I. De Looze[3], J. Fritz[3], G. Gavazzi[6], C. Giovanardi[1], M. Grossi[7], L. K. Hunt[1], L. Magrini[1], D. Pierini[8], and E. M. Xilouris[9]

[1] INAF-Osservatorio Astrofisico di Arcetri, L.go E. Fermi 5, 50125 Firenze, Italy
e-mail: sperello@arcetri.astro.it
[2] School of Physics and Astronomy, Cardiff University, The Parade, Cardiff, CF24 3AA, UK
[3] Sterrenkunding Observatorium, Universiteit Gent, Krijgslaan 281 S9, 9000 Gent, Belgium
[4] UK ALMA Regional Centre Node, Jodrell Bank Centre for Astrophysics, School of Physics and Astronomy, University of Manchester, Oxford Road, Manchester M13 9PL, UK
[5] European Southern Observatory, Karl-Schwarzschild Str. 2, 85748 Garching bei München, Germany
[6] Universitá di Milano – Bicocca, Piazza delle Scienze 3, 20126 Milano, Italy
[7] CAAUL, Observatòrio Astronòmico de Lisboa, Tapada de Ajuda, 1349-018 Lisboa, Portugal
[8] Max-Planck-Institut für Extraterrestrische Physik, Gießenbachstraße, Postfach 1312, 85741 Garching, Germany
[9] Institute for Astronomy, Astrophysics, Space Applications & Remote Sensing, National Observatory of Athens, P. Penteli, 15236 Athens, Greece

Received 12 October 2012 / Accepted 10 January 2013

ABSTRACT

Aims. We study the dust content of a large optical input sample of 910 early-type galaxies (ETG) in the Virgo cluster, also extending to the dwarf ETG, and examine the results in relation to those on the other cold ISM components.
Methods. We have searched for far-infrared emission in all galaxies in the input sample using the 250 μm image of the *Herschel* Virgo Cluster Survey (HeViCS). This image covers a large fraction of the cluster with an area of ~55 square degrees. For the detected ETG we measured fluxes in five bands from 100 to 500 μm, and estimated the dust mass and temperature with modified black-body fits.
Results. Dust is detected above the completeness limit of 25.4 mJy at 250 μm in 46 ETG, 43 of which are in the optically complete part of the input sample. In addition, dust is present at fainter levels in another six ETG. We detect dust in the four ETG with synchrotron emission, including M 87. Dust appears to be much more concentrated than stars and more luminous ETG have higher dust temperatures. Considering only the optically complete input sample and correcting for the contamination by background galaxies, dust detection rates down to the 25.4 mJy limit are 17% for ellipticals, about 40% for lenticulars (S0 + S0a), and around 3% for dwarf ETG. Dust mass does not correlate clearly with stellar mass and is often much greater than expected for a passive galaxy in a closed-box model. The dust-to-stars mass ratio anticorrelates with galaxy luminosity, and for some dwarf ETG reaches values as high as for dusty late-type galaxies. In the Virgo cluster slow rotators appear more likely to contain dust than fast ones. Comparing the dust results with those on HI there are only eight ETG detected both in dust and in HI in the HeViCS area; 39 have dust but only an upper limit on HI, and eight have HI but only an upper limit on dust. The locations of these galaxies in the cluster are different, with the dusty ETG concentrated in the densest regions, while the HI rich ETG are at the periphery.

Key words. galaxies: elliptical and lenticular, cD – galaxies: clusters: general – galaxies: ISM – dust, extinction

1. Introduction

Dust is a very important component of galaxies, since it is closely connected with their evolution (Draine 2003). Dust is thought to be the product of the last stages of the evolution of low- and intermediate-mass stars, of supernovae (SN), and possibly also of active galactic nuclei (AGN). After dust is formed, how much of it survives in the interstellar medium (ISM) depends on specific local conditions, and dust can also grow directly in the ISM. The presence of dust has a profound effect on galaxy colours by absorbing blue/UV radiation and re-emitting it in the InfraRed (IR), therefore influencing the amount of escaping ionising radiation. Together with cold gas, dust is associated with regions of star formation (SF), so that dust emission is often used as a tracer for SF. Finally, since dust can be destroyed by the energetic ions in hot haloes and can serve as a catalyzer for the formation of molecules, its presence (or absence) can provide important clues to the relationships between the different phases of the ISM.

Early-type galaxies (ETG) are spheroidal and bulge-dominated galaxies, including ellipticals (E), lenticulars (S0 and S0a), and dwarf spheroidals (dE and dS0). They contain most of the visible mass in the Universe, and are a uniform class of galaxies with a relatively simple morphology and smooth kinematics. They were thought to be devoid of ISM, but in the last decades were found instead to contain a multiform ISM. Its richest component in massive ETG is hot gas, visible in X-rays,

⋆ *Herschel* is an ESA space observatory with science instruments provided by European-led Principal Investigator consortia and with important participation from NASA.
⋆⋆ Table A.1 is available in electronic form at http://www.aanda.org

but cooler phases are also present, down to the coldest ones, i.e. molecular gas and dust (Roberts et al. 1991). In particular the systematic study of the dust content in ETG can provide important clues to the survival of the cold ISM phases in the harsh environment produced by the hot gas (and in some cases by the central AGN), to the presence of residual SF, and to the exchanges of ISM between an ETG and the surrounding intergalactic medium (IGM) or other galaxies, throughout its evolution.

The presence of dust in ETG can also change their appearance in subtle ways (Witt et al. 1992). For example, colour gradients resulting from dust reddening can mimic those due to metallicity gradients. In addition, Baes & Dejonghe (2001, 2002) have suggested that dust scattering can affect the observed kinematics of elliptical galaxies, even mimicking the signature of a dark matter halo. Therefore, it is crucial to have an extinction-independent way to evaluate the amount of dust in ETG, also in order to properly understand their other properties.

The presence of dust in ETG was first inferred from the absorption of stellar light (Bertola & Galletta 1978; Ebneter & Balick 1985; Goudfrooij et al. 1994). Dust lanes are easy to find on the very smooth light profiles of elliptical galaxies. However, dust absorption does not say much about the quantitative dust content of ETG. Far-infrared (FIR) emission from dust in ETG was later observed with the InfraRed Astronomical Satellite (IRAS) in about 45% of ellipticals and 68% of S0 galaxies (Knapp et al. 1989). More recently Temi et al. (2004) detected FIR dust emission with the Infrared Space Observatory (ISO) from about 55% of a sample of 53 bright ETG, with dust masses ranging from 10^5 to more than 10^7 solar masses. Using the *Spitzer* Space Telescope, Temi et al. (2007) found evidence for extended diffuse dust in a similar sample of ETG. Others have used ground-based telescopes to measure the dust emission on a few bright ETG (Leeuw et al. 2004; Savoy et al. 2009). However, these observations are limited to relatively small samples of very bright ETG and lack the sensitivity, the resolution, and/or the long wavelength coverage necessary to study dust in large samples of ETG including dwarf galaxies.

The *Herschel* Virgo Cluster Survey (HeViCS, Davies et al. 2010, 2012), a confusion-limited imaging survey of a large fraction of the Virgo cluster in five bands – 100 and 160 μm with PACS (Poglitsch et al. 2010) and 250, 350 and 500 μm with SPIRE (Griffin et al. 2010) – offers the unique opportunity of carrying out a complete analysis of the dust content of ETG in a nearby cluster. Auld et al. (2012) have searched the HeViCS images for FIR counterparts of Virgo cluster galaxies of all morphological types with photographic magnitude $m_{pg} \leq 18.0$. The present study instead is limited to ETG, but has no limit on the optical magnitude. Our work is also complementary to the one by Smith et al. (2012) on the ETG of the *Herschel* Reference Survey (HRS, Boselli et al. 2010b). This research has searched dust in 62 bright ETG, i.e. a volume-limited sample ($15 < d < 25$ Mpc) including the Virgo cluster, with $K \leq 8.7$, a bright limit, corresponding to a stellar mass of about 10^{10} $M_\odot$. Although it is limited to massive galaxies, the HRS sample has the advantage of also including field galaxies. On the other hand, with HeViCS we can also study galaxies which are 1000 times less massive than the HRS limit, but we are limited to the Virgo cluster environment.

In Sect. 2 we discuss the selection of the optical input sample, while in Sect. 3 we describe the methods and the results for the detection and photometry of the dusty ETG. Important quantities are derived from the observed parameters in Sect. 4. Discussions and conclusions are presented in Sects. 5 and 6.

2. Sample selection

The sample of ETG to be searched for dust within HeViCS was selected at optical wavelengths using the GOLDMine compilation (Gavazzi et al. 2003), which is mostly based on the Virgo Cluster Catalogue (VCC, Binggeli et al. 1985, 1993), including all morphological types from −3 to 2 (i.e. galaxies earlier than S0a-S0/Sa) and excluding galaxies with radial velocity larger than 3000 km s^{-1}, since these are background galaxies; we have retained galaxies without a measured radial velocity. With these selection criteria, 925 ETG are within the 4 HeViCS fields. These galaxies constitute our input sample. This includes a large fraction (73.7%) of all the known Virgo ETG (GOLDMine has 1255 Virgo galaxies with types from −3 to 2 and radial velocity not larger than 3000 km s^{-1}), thereby confirming that the HeViCS fields cover most of the Virgo cluster.

We start from an accurate central position for every ETG in the input catalogue, which we obtained mostly from NED[1]. However, for 287 ETG of our input sample, NED has positions accurate to 25 arcsec, both in RA and in Dec, which are based only on the original work of Binggeli et al. (1985). This accuracy is insufficient for a reliable search of a possible counterpart in the HeViCS mosaic image at 250 μm, which has a pixel size of 6 arcsec, a point-spread function (PSF) with full width at half maximum (FWHM) of 18 arcsec, and a very high density of objects. We have therefore measured new accurate positions for these 287 objects, using the Gunn *r*-band image of the Sloan Digital Sky Survey (SDSS). We succeeded in measuring 272 (all except 15) with $m_{pg} > 19.0$ (see Appendix A). Therefore, we could reliably look for a FIR counterpart for 910 ETG of our input sample of 925. Out of the 910 ETG of the input sample, 447 ETG are brighter than the VCC completeness limit ($m_{pg} \leq 18.0$) and form the optically complete part of our input sample.

3. Methods and results

3.1. Detection and photometry

We searched for a FIR conterpart of the 910 ETG of the input sample in the HeViCS 8-scan mosaic image at 250 μm. We did a blind search for sources in the 250 μm mosaic, using both the DAOPhot and SussExtractor implementations in HIPE (Ott 2010), which produce equivalent results. We then searched the resulting catalogue of sources for those corresponding to the optical positions of the 910 ETG with accurate coordinates in our input catalogue within one pixel (6 arcsec) and with a signal-to-noise ratio greater than 5 ($S/N > 5$). The resulting candidate counterparts were then examined in detail to establish the reliability of the galaxy detection in the 250 μm image and of its identification with the ETG in the input sample. For the last step we overlayed the 250 μm image with an optical image of the galaxy. This procedure gave a list of 52 reliable FIR counterparts, all at $S/N > 6$. For all of them the separation between the optical centre of the galaxy and that of its FIR counterpart is ≤5 arcsec. For these ETG we measured the flux using the aperture photometry package in the Image Reduction and Analysis Facility (IRAF, Tody 1993) with an aperture of 30 arcsec radius, large enough to include most of the PSF also at 500 μm, by centering the aperture on the detected counterpart, and by subtracting the sky background evaluated in a concentric annulus with

[1] The NASA/IPAC Extragalactic Database (NED) is operated by the Jet Propulsion Laboratory, California Institute of Technology, under contract with the National Aeronautics and Space Administration.

Table 1. Early-type galaxies detected with HeViCS in the complete FIR detection sample.

VCC	Other name	RA	Dec	Type	m_{pg}	Dist.	Ap. Rad.	F_{100}	F_{160}	F_{250}	F_{350}	F_{500}
		h m s	° ′ ″	GM[1]		Mpc	arcsec	mJy	mJy	mJy	mJy	mJy
94	NGC 4191	12 13 50.40	+07 12 03.2	2	13.57	32.0	42	<300	493	312	156	46
165		12 15 53.28	+13 12 57.1	1	14.87	17.0	30	71	207	167	73	16
209	IC 3096	12 16 52.36	+14 30 52.5	–3	15.15	17.0	30	187	313	221	114	41
218	IC 3100	12 17 05.55	+12 17 23.4	–3	14.88	17.0	30	<32	86	45	13	<15
220	NGC 4233	12 17 07.68	+07 37 27.8	1	12.97	32.0	30	192	<178	168	73	35
270		12 18 06.81	+05 41 04.3	2	15.02	32.0	30	252	232	130	46	12
278		12 18 14.42	+06 36 13.1	–3	15.1	23.0	30	149	<200	32	11	6
292		12 18 31.72	+05 50 59.3	–1	17.0	32.0	30	<32	36	26	23	10
312	NGC 4255	12 18 56.15	+04 47 10.1	1	13.61	32.0	30	53	74	59	30	13
327		12 19 12.38	+06 22 53.7	1	14.8	32.0	30	88	130	107	50	18
345	NGC 4261	12 19 23.22	+05 49 30.8	0	11.31	32.0	30	294	192	199	179	149
408	NGC 4281	12 20 21.52	+05 23 11.0	1	12.27	32.0	30	1282	1275	579	217	70
411	NGC 4282	12 20 24.31	+05 34 22.2	1	14.53	23.0	30	268	265	201	90	28
450		12 21 03.65	+07 04 39.6	1	15.08	23.0	30	324	309	190	90	29
462	NGC 4292	12 21 16.46	+04 35 44.5	2	13.5	17.0	30	851	866	499	199	60
482		12 21 34.08	+04 46 46.3	2	14.77	17.0	30	<32	41	27	24	16
498		12 21 43.31	+10 14 02.6	–1	18.5	17.0	30	73	44	26	16	<15
571		12 22 41.16	+07 57 01.3	1	14.74	23.0	30	61	124	96	63	26
622		12 23 10.92	+09 01 43.4	–1	16.7	23.0	30	<32	24	35	20	<15
672	NGC 4341	12 23 53.56	+07 06 25.6	1	14.21	23.0	30	214	214	133	64	25
685	NGC 4350	12 23 57.87	+16 41 36.3	1	11.99	17.0	30	1536	<1200	318	114	22
705		12 24 10.96	+11 56 47.3	–1	17.2	17.0	30	<32	44	38	22	14
710		12 24 14.52	+04 13 33.4	–3	14.83	17.0	30	85	141	119	68	31
758	NGC 4370	12 24 54.90	+07 26 41.6	1	13.69	23.0	48	3071	3601	1949	782	252
763	NGC 4374	12 25 03.74	+12 53 13.1	0	10.26	17.0	30	932	652	265	146	106
764		12 25 05.61	+05 19 44.8	1	14.9	17.0	30	59	163	73	41	<15
781	IC 3303	12 25 15.20	+12 42 52.6	–3	14.72	17.0	30	165	91	88	51	20
788		12 25 16.83	+11 36 19.2	–1	15.8	17.0	30	<60	<58	29	14	<15
832		12 25 43.58	+12 40 27.5	–1	19.0	17.0	30	17	49	38	18	<15
881C	NGC 4406	12 26 10.65	+12 56 23.2	0	10.06	17.0	42	200	282	130	62	24
881SE		12 26 13.64	+12 54 51.2			17.0	51	<54	221	273	168	71
951	IC 3358	12 26 54.34	+11 39 50.3	–2	14.35	17.0	30	179	143	110	54	19
1003	NGC 4429	12 27 26.51	+11 06 27.8	2	11.15	17.0	42	4436	4523	2107	703	198
1030	NGC 4435	12 27 40.49	+13 04 44.2	1	11.84	17.0	48	4225	3804	1897	748	237
1154	NGC 4459	12 29 00.01	+13 58 42.1	1	11.37	17.0	48	4420	3738	1708	617	183
1226	NGC 4472	12 29 46.76	+08 00 01.7	0	9.31	17.0	66	<68	396	86	106	52
1250	NGC 4476	12 29 59.08	+12 20 55.2	1	12.91	17.0	42	1507	1435	751	287	103
1253	NGC 4477	12 30 02.20	+13 38 11.8	2	11.31	17.0	42	1215	1057	472	178	40
1316	NGC 4486	12 30 49.42	+12 23 28.0	0	9.58	17.0	54	580	825	806	1033	1281
1420	IC 3465	12 32 12.24	+12 03 41.6	–1	16.41	17.0	30	62	<78	73	62	27
1512		12 33 34.66	+11 15 43.0	–3	15.73	17.0	30	<92	157	46	19	8
1535	NGC 4526	12 34 03.03	+07 41 56.9	1	10.61	17.0	78	15 835	15 637	7992	3160	1038
1578		12 34 41.68	+11 08 34.1	–1	19.7	17.0	30	49	<58	29	30	18
1614	IC 3540	12 35 27.23	+12 45 00.9	1	14.44	17.0	30	52	89	30	<19	<15
1619	NGC 4550	12 35 30.58	+12 13 15.0	0	12.5	17.0	30	193	306	133	45	6
1632	NGC 4552	12 35 39.81	+12 33 22.8	1	10.78	17.0	30	121	<98	28	30	20
1684	IC 3578	12 36 39.41	+11 06 06.7	–3	14.87	17.0	30	21	41	30	12	<15

Notes. GOLDMine type: –3=dS0 –2=dE/dS0 –1=dE(d:E) 0=E-E/S0 1=S0 2=S0a-S0/Sa.

an inner radius of 48 arcsec and an outer radius of 78 arcsec. Table 1 lists the 46 ETG with a 250-μm flux above our completeness limit of 25.4 mJy. This limit is determined via Monte Carlo simulations to be the flux at which the success rate in recovering artificial point-like sources drops below 95%. Out of these 46 ETG, 43 belong to the optically complete input sample (i.e. they have $m_{pg} \leq 18.0$), and they represent our complete FIR counterparts out of the complete input optical sample of ETG. The other 6 ETG with an evident counterpart in the 250 μm image have a 250-μm flux slightly smaller than 25.4 mJy, and are listed separately in Table 2. All of them are detected in at least one other HeViCS band. We remark that the choice of measuring fluxes using an aperture of 30 arcsec in all bands in order to have a consistent SED implies that at 250 μm this photometric aperture is larger than required for pure detections. Therefore, although all of our 46 counterparts that are brighter than the completeness limit are reliably detected at $S/N > 6$, for some of them the photometric flux measurement is at a lower signal-to-noise ratio (S/N, see the discussion on photometric errors below).

During the visual examination step we noticed that a few of the detected ETG also had 250 μm emission outside the 30 arcsec aperture. For these ETG we did the photometry using a larger aperture (see Tables 1 and 2) which includes all the visible FIR flux. For these larger apertures the sky annulus was correspondingly larger. The same apertures and sky annuli were also used for the photometry in the other HeViCS bands

Table 2. Additional early-type galaxies detected with HeViCS.

VCC	Other name	RA h m s	Dec ° ′ ″	Type GM[1]	m_{pg}	Dist. Mp	Ap. Rad. arcsec	F_{100} mJy	F_{160} mJy	F_{250} mJy	F_{350} mJy	F_{500} mJy
150		12 15 28.57	+12 38 51.5	–1	20.0	17.0	30	<32	<18	13	20	6
486	IC 782	12 21 36.97	+05 45 56.7	2	14.5	23.0	30	34	42	18	13	<15
1175		12 29 18.20	+10 08 09.0	0	16.01	23.0	30	14	38	19	15	<15
1327	NGC 4486A	12 30 57.71	+12 16 13.3	0	13.26	17.0	30	155	82	13	<19	<15
1706		12 37 11.31	+12 26 46.1	–1	20.0	17.0	30	<32	<18	23	11	<15
1715		12 37 28.52	+08 47 40.3	–1	16.2	17.0	30	<32	67	21	<19	<15

Notes. GOLDMine type: –3=dS0 –2=dE/dS0 –1=dE(d:E) 0=E-E/S0 1=S0 2=S0a-S0/Sa.

for all the 52 ETG detected at 250 μm. For the SPIRE bands (250, 350, and 500 μm) we did the photometry on the mosaic images, which include the 4 HeViCS fields, since these handle well objects which fall in the region of overlap between two fields. Figure 1 shows all the 52 ETG detected at 250 μm.

For the PACS bands (at 100 and 160 μm) we used the images produced for the most recent HeViCS data release (Auld et al. 2013), which represents for our purposes a substantial improvement over previous releases. A low-pass filter is used for the removal of background noise and instrumental drift. Bright sources have to be masked out before applying the filter to avoid producing a flux reduction around these. The most recent release masks out all catalogued Virgo galaxies, as well as all the bright sources present in the data. This process prevents the problem of flux reduction for all the sources in our input catalogue. Since mosaic images are not available for PACS, we performed the photometry on the individual images for each of the four HeViCS fields. Although the PACS photometry on the 52 ETG was done blindly using the same aperture used at 250 μm, every ETG was examined visually in each HeViCS band and flagged in case it was not detected in that band, in which case a flux upper limit appears in Tables 1 and 2.

In the case of VCC 881 (M 86, NGC 4406) we used two circular photometric apertures: one with a radius of 42 arcsec, containing the central dust emission, centred slightly to the south-west of the nucleus (VCC 881C), and one with a radius of 51 arcsec, containing the emission from the filament at about 2 arcmin to the south of the nucleus (VCC 881SE), based on the information on the dust content collected during the HRS Science Demonstration phase (Gomez et al. 2010).

The methods followed for the photometric error analysis are dictated by the scope of our work, which is aperture photometry of generally faint and compact sources, detected by the use of well-known source-extraction algorithms and checked by visual inspection. We take into account the stochastic pixel-to-pixel fluctuations in randomly selected sky regions free of bright sources and their effect on our relatively small apertures. These take into account the background error, instrumental noise, and confusion noise. In SPIRE on reasonably clean sky areas we measure 1-σ pixel-to-pixel fluctuations of 4.9, 4.9, and 5.7 mJy/beam at 250, 350, and 500 μm, respectively (beam areas are 423, 751, and 1587 arcsec^2, and pixel sizes are 6, 8, and 12 arcsec). In PACS we measure pixel-to-pixel 1-σ fluctuations of 0.6 and 0.5 mJy/pix at 100 and 160 μm, respectively (pixel sizes are 2 and 3 arcsec). Therefore, in our standard 30 arcsec aperture we adopt a 1-σ error of 12.7, 9.5, 7.6, 16.0, and 8.9 mJy at 250, 350, 500, 100, and 160 μm, respectively. For larger apertures we assume that the noise increases as the square root of the number of pixels. Calibration errors (7% for SPIRE and 15% for PACS) are added in quadrature to obtain the total photometric error.

Table 3. Background galaxy contamination at 250 μm.

Flux bin mJy	n_{BGi} arcsec^{-2}	N_{BGi}	N_{det}
25.4–40.3	6.16×10^{-5}	4.4	11
40.3–63.8	3.44×10^{-5}	2.5	4
63.8–101.1	1.10×10^{-5}	0.78	5
101.1–160.3	2.43×10^{-6}	0.17	6
160.3–254.0	6.66×10^{-7}	0.050	6
254.0–402.6	2.22×10^{-7}	0.016	3
402.6–638.0	1.43×10^{-7}	0.010	4
638.0–∞	2.43×10^{-7}	0.018	7
25.4–∞	1.11×10^{-4}	7.90	46

Tables 1 and 2 list the fluxes measured in all five bands and the radius of the circular aperture used consistently in all bands. For the undetected sources an upper limit is given, which is generally equal to twice the photometric error. In noisy regions we give correspondingly higher upper limits.

3.2. Contamination by background sources

Since the SPIRE 250 μm image that we used to search for the FIR counterparts has a high density of background sources, we have estimated the fraction of our counterparts that are probably background galaxies. We do so in flux bins which are spaced logarithmically by 0.2 (a factor of 1.585). The number of probable background galaxies among our counterparts in the ith flux bin is:

$$N_{BGi} = n_{BGi} \times N_{opt} \times \pi r_{max}^2, \quad (1)$$

where n_{BGi} is the density of background sources that we have estimated from SussExtractor counts in the HeViCS 250 μm mosaic image, N_{opt} is the total number of optically selected galaxies in our input sample, i.e. 910, and r_{max} is the maximum angular separation between the optical centre of each dust-detected galaxy and the centre of the FIR counterpart, i.e. 5 arcsec (see Sect. 3.1). Table 3 lists the relevant parameters for the background galaxy contamination including the number of detected ETG for each flux bin (N_{det}). Since we estimated the density of background sources n_{BGi} from the HeViCS mosaic, its value at higher flux bins contains an increasing fraction of Virgo galaxies. However, this problem does not substantially affect our estimate of the contamination due to background sources since the contamination is relevant only for the lowest flux bins that contain a negligible fraction of Virgo galaxies.

The result is that about 8 background galaxies are probably contaminating the 46 detections listed in Table 1; 7 of these

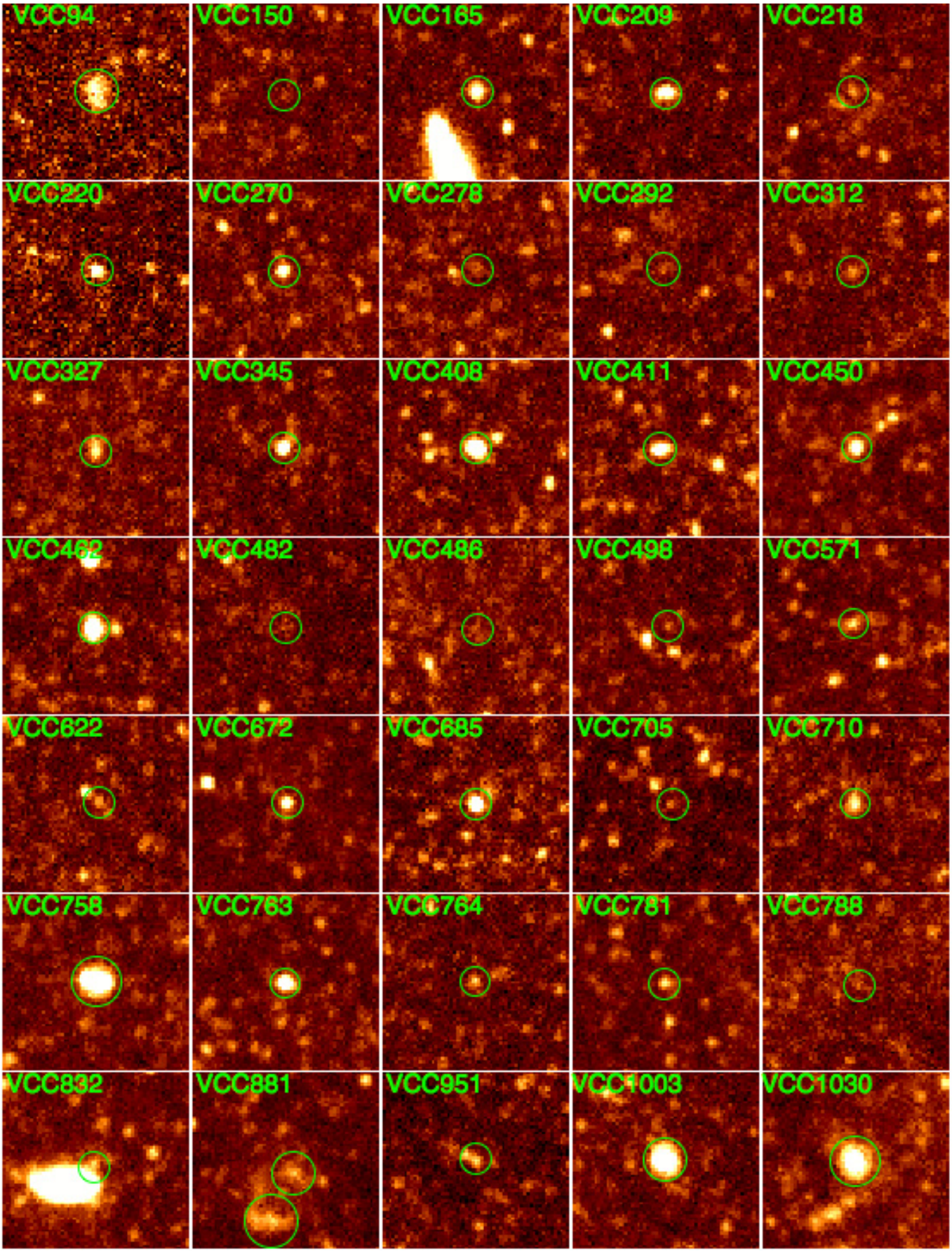

Fig. 1. Images at 250 μm of all the 52 detected ETG. For each image north is up, east to the left, and the size is 6 arcmin. The green circles are the apertures used for flux measurements.

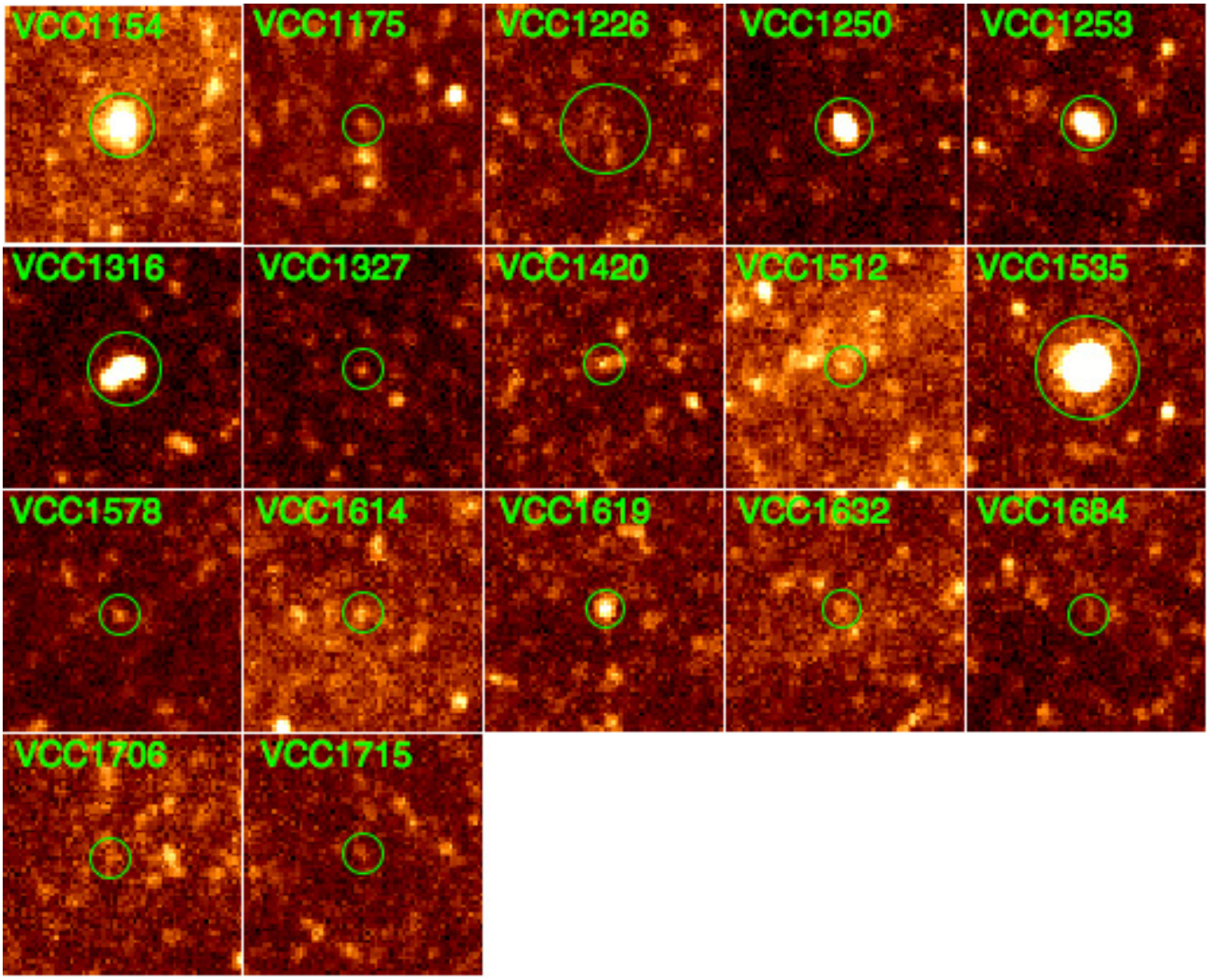

Fig. 1. continued.

are in the two lowest flux bins, which contain 11 dwarf galaxies and 4 lenticulars detected at 250 μm. Therefore in our Virgo ETG sample between 4 and 8 dwarf galaxies, out of a total of 16, and between 0 and 4 lenticulars, out of a total of 24, are likely spurious FIR detections. Assuming that the contamination rate is roughly independent of $m_{\rm pg}$, the expected number of contaminants in the optically complete sample is about half of the total (447/910). This statistical contamination, however, does not affect the main results of our work.

In the context of possible spurious identifications with background sources, VCC 815 deserves a special mention, since we do detect a FIR source near the position of VCC 815; however, we think that this source is not associated with the VCC galaxy, but with a redder background galaxy. Binggeli et al. (1985) had already noticed this background galaxy to the west of VCC 815, and attributed a redshift of $v_{\rm Hel}$ = 16 442 km s^{-1} to it, refering to a private communication by Huchra. Indeed, the position of the background galaxy, clearly visible on the SDSS images, coincides exactly with that of the HeViCS 250 μm detection, while VCC 815 is at about 5 arcsec to the east.

3.3. Comparison with other work

Auld et al. (2013) have used HeViCS data to study the dust content of the complete part of the VCC, i.e. of those galaxies with $m_{\rm pg} \leq 18.0$, including all morphological types. Of the common complete sample we have detected all of the 42 sources detected by Auld et al. (two are in VCC 881, i.e. M 86). In addition, we have also detected 6 ETG of the Auld et al. (2013) sample, which they did not detect: VCC 218, 482, 705, 1226, 1420, and 1684. Our photometry agrees with that of Auld et al., particularly if one considers that different photometric methods were followed. For the 42 sources detected in both papers the fluxes are consistent within the given errors, while for the sources detected only by us, the measured fluxes are compatible with the upper limits given by Auld et al., except for VCC 705, for which Auld et al. used the coordinates from Binggeli et al. (1985), which we have found to be inaccurate (see Appendix A). Finally, we have detected an additional 5 ETG fainter than $m_{\rm pg}$ = 18.0, which were not in the Auld et al. input sample.

Smith et al. (2012) have looked at the 62 ETG of the *Herschel* Reference Survey (Boselli et al. 2010b). The HRS collaboration has obtained *Herschel* observations of a volume-limited sample (distance between 15 and 25 Mpc) of 323 bright local galaxies ($K \leq 8.7$), including the Virgo cluster. For the galaxies of this cluster the HRS project shares the SPIRE data with HeViCS. Our input sample has 25 ETG in common with the input sample of Smith et al. We detect dust in all of the 9 ETG (2 E and 7 S0) for which Smith et al. detect dust;

in addition we detect dust in VCC 1226 (M 49, NGC 4472, HRS 178), VCC 1316 (M 87, NGC 4486, HRS 183), and VCC 1632 (NGC 4552, HRS 211), which Smith et al. consider non-detections. Our photometry for these 3 ETG is consistent with the upper limits of Smith et al. (2012). The fluxes measured in the SPIRE bands for the common sources are generally consistent within the given errors, although they were measured with different photometric methods. Analysing the reasons for the small differences between Smith et al. (2012) and this work, we remark that their methods were optimised for bright galaxies and are explained in detail by Ciesla et al. (2012). They adopt a different photometric method for the point-like sources and for the extended ones. For the first they fit a Gaussian function on the timeline data, while for the latter they do aperture photometry on the reconstructed images, using larger apertures than we did. Although Gaussian fitting of timeline data is likely to give the best S/N for true point sources, we have adopted the same size aperture in all bands and for all objects, because adopting two systematically different methods may compromise photometric uniformity. Moreover, since our sources are galaxies, they may have flux outside the PSF.

4. Derived quantities

In this section we estimate additional important physical quantities and describe how they are derived. These depend on the assumed distance: for each galaxy we have used the distance given in GOLDMine (17, 23, or 32 Mpc), which distinguishes various components of the Virgo cluster (Gavazzi et al. 1999).

4.1. Dust mass and temperature

Dust masses and temperatures were estimated by fitting a modifed black-body to the measured HeViCS fluxes for each galaxy. In the case of M 86 (VCC 881), separate estimates were performed for the two regions which we measured separately (see Sect. 3). We used the same procedure as described in Magrini et al. (2011, see also Smith et al. 2010; Davies et al. 2012). We assumed a spectral index $\beta = 2$ and an emissivity $\kappa[\mathrm{cm}^2/\mathrm{g}] = 0.192 * (350\,\mu\mathrm{m}/\lambda)^2$, as derived from the Galactic dust emission (Draine 2003); we took into account the filter response function to derive the colour correction. Given the compactness of our sources, for SPIRE we assumed the filter response function for point sources; more details and a table of colour corrections are given in Davies et al. (2012).

We also applied aperture correction factors according to Griffin (priv. comm., see also Auld et al. 2013). For our smallest aperture (30 arcsec radius) these are 1.02, 1.05, 1.13, 1.15, and 1.27 at 100, 160, 250, 350, and 500 μm, respectively.

Figure 2 shows the modified back-body fits and Table 4 lists the estimated dust masses and temperatures. For the 14 galaxies for which flux measurements could be made in only 3 bands or fewer, or for which the temperature is not accurately estimated, we have fixed the dust temperature at the average value obtained for the galaxies with the same GOLDMine morphological type (see Fig. 3). These average temperature values are: $T = 17.6 \pm 0.7, 15.6 \pm 0.8, 21.3 \pm 0.4, 21.2 \pm 3.8, 21.4 \pm 3.5$ K for GOLDMine types −3, −1, 0, 1, 2, respectively. In these cases the error given for the dust mass in Table 4 takes also into account the variance on the average temperature in the given morphological class. Figure 4 shows the modified black-body fits obtained at the fixed temperature, and results are listed in Table 4.

By using these average dust temperatures, which we have obtained for each morphological class, it is possible to put upper limits to the dust mass of all the 868 Virgo ETG that fall in the HeViCS fields but have not been detected at 250 μm, by taking into account the upper limit of $F_{250} \leq 25.4$ mJy

$$M_{\mathrm{dust}} \leq \alpha \times 25.4 \times 10^4\ M_{\odot} \times (\mathrm{Distance}/17\ \mathrm{Mpc})^2, \quad (2)$$

where $\alpha = 0.42, 0.70, 0.21, 0.38, 0.34$, for GOLDMine types −3, −1, 0, 1 and 2 respectively, including the effect of the variance in the average dust temperature. Dust mass upper limits for the ETG not detected in HeViCS at 17 Mpc, the distance of the main Virgo cloud, range between 5 and $18 \times 10^4\ M_{\odot}$, depending on the morphological type, and are correspondingly larger at greater distances.

Four of the ETG detected in HeViCS are known radio sources (VCC 345, 763, 1316, and 1632). The influence of the synchrotron radiation in the HeViCS bands is evident for these objects, particularly at longer wavelengths, and was already seen in *Herschel* data for VCC 763 (M 84, Boselli et al. 2010a) and VCC 1316 (M 87, Baes et al. 2010). For these objects the fit, in addition to a modified black-body, also includes a synchrotron component, whose slope is fixed at the radio slope (see Fig. 5). For VCC 345, 1316, and 1632, in the fit we fixed the dust temperature at the average temperature obtained for ETG of the same morphological class (see above), since it could not be reliably determined by the fit itself. All 4 sources show the presence of dust emission, in addition to the synchrotron component; this is also true for M 87, for which our aperture includes both the nucleus and the jet. In M 87 our detection is consistent with the upper limit of Baes et al. (2010), who did not detect dust in the lower quality HeViCS Science Demonstration 2-scan data. We have checked that for each of the four galaxies the amplitude of the fitted synchrotron component agrees well with the radio data, within the uncertainties due to the different apertures used in the radio and in the FIR.

The presence of dust in these radio-loud objects is not completely new, since dust filaments were seen in absorption in the central arcminute of M 87 by Sparks et al. (1993), who suggest a dust-to-gas ratio close to the Galactic value. The presence of dust in M 87 was also suggested by Xilouris et al. (2004) by combining their ISO data at 4.5, 6.7, and 15 μm with IRAS data at 60 and 100 μm, using an aperture very similar to ours. Their estimate gives a smaller quantity of dust at a higher temperature. The possible presence of dust near the nucleus of M 87 was inferred from spectroscopic observations with *Spitzer* IRS, which showed an excess emission over the synchrotron component between 30 and 34 μm, the longest observed wavelengths (Perlman et al. 2007). An alternative analysis of IRS spectra by Buson et al. (2009) in the region up to 24 μm found no sign of dust emission: their MIR spectrum up to 24 μm can be completely explained by a combination of a stellar contribution and a synchrotron component. It is difficult to compare in detail these dust detections with ours for several reasons. First Perlman et al. had a much smaller aperture, about 10 arcsec vs. our 54 arcsec. In addition, they model their excess with a dust component at $T \approx 55$ K, which would contribute less than half of the flux that we have observed at 100 μm, while our dust component has a negligible contribution to the *Spitzer* IRS spectrum. It is possible, however, that Xilouris et al. and Perlman et al. have seen warmer dust closer to the nucleus, while we are seeing colder dust over a larger volume. A new analysis of the MIR-FIR-radio SED of M 87, including new and deeper *Herschel* imaging data, is forthcoming (Baes et al., in prep.).

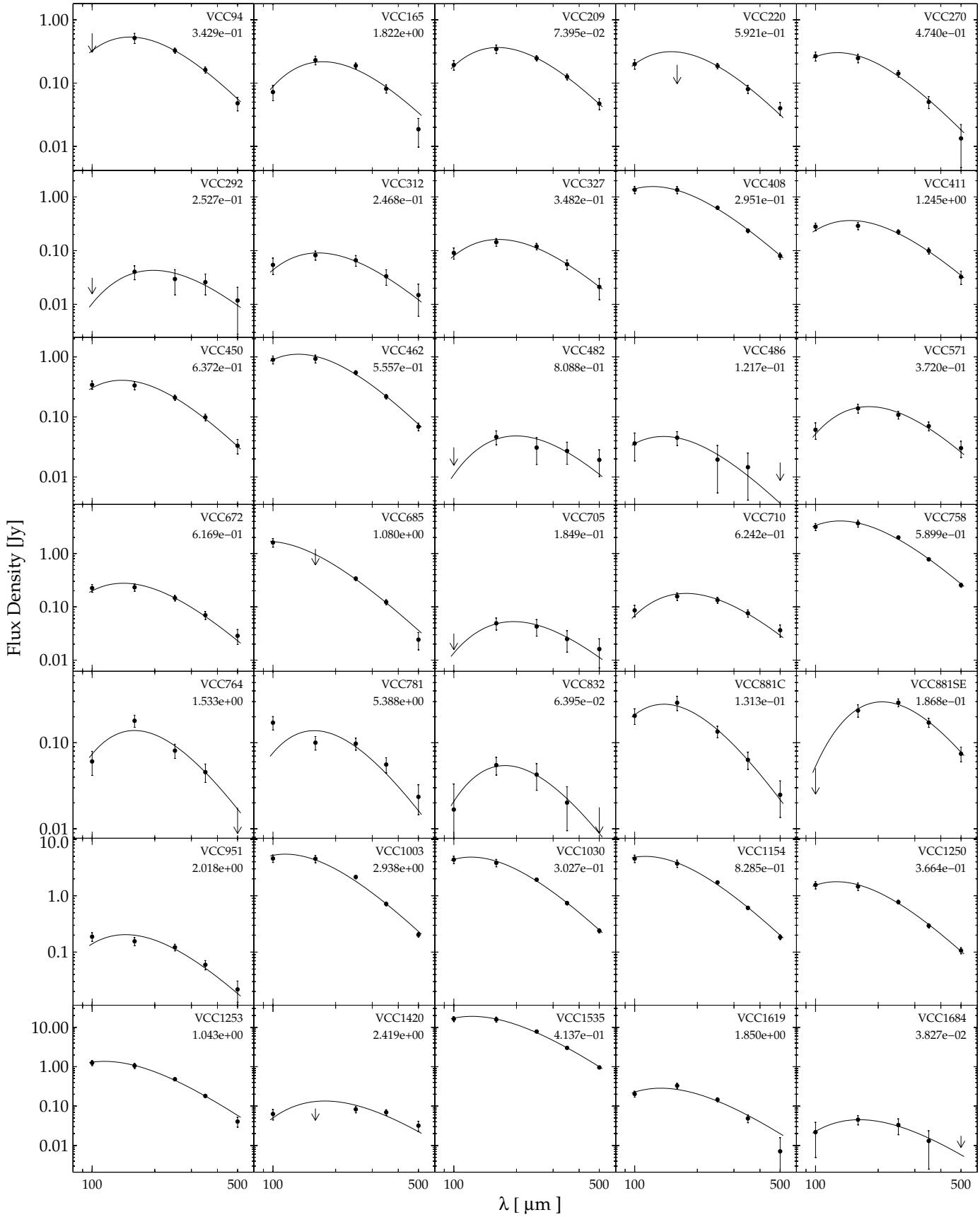

Fig. 2. Modified black-body fits to the HeViCS fluxes for all the detected ETG for which fits could be done with temperature as a free parameter and without synchrotron emission. The χ^2 of each fit is listed under the object name. Upper limits to the fluxes are shown by downward arrows.

Table 4. Derived quantities for the early-type galaxies detected with HeViCS.

VCC	Type GM	M_B	Dist. Mpc	M_{dust} $10^4\ M_\odot$	T_{dust} K	M_{star} $10^8\ M_\odot$	Bands for M_{star}	M_{HI} $10^7\ M_\odot$	M_{H_2} $10^7\ M_\odot$	Ref. $(H_2)^c$
94	2	–19.04	32.0	325 ± 83	19.1 ± 1.5	133 ± 40	BVH	180.2	<9	Y11
150	–1	–11.30	17.0	13.5 ± 6.7	15.6[a]	0.049 ± 0.013	gi	<3.6		
165	1	–16.42	17.0	72 ± 13	16.7 ± 0.7	9.9 ± 4.4	BH	<7.9		
209	–3	–16.14	17.0	87 ± 13	17.9 ± 0.6	3.4 ± 0.9	giH	3.9		
218	–3	–16.41	17.0	20.1 ± 4.0	17.6[a]	2.7 ± 1.8	BH	<3.6		
220	1	–19.66	32.0	176 ± 30	19.4 ± 0.8	334 ± 98	BVH	<27.9	<8	Y11
270	2	–17.59	32.0	76 ± 16	22.8 ± 1.2	25 ± 13	BH	<27.9		
278	–3	–16.81	23.0	31 ± 7	17.6[a]	10 ± 5	BH	<6.6		
292	–1	–15.60	32.0	49 ± 37	14.7 ± 2.3	2.3 ± 0.6	gi	<12.9		
312	1	–19.00	32.0	83 ± 33	17.6 ± 1.5	206 ± 92	BH	<27.9	<6	Y11
327	1	–17.81	32.0	142 ± 35	17.7 ± 0.9	7.0 ± 4.7	BH	<27.9		
345	0	–21.29	32.0	64 ± 5[b]	21.3[a]	2079 ± 198	BVH	<27.9	<5	C07
408	1	–20.34	32.0	314 ± 37	23.8 ± 0.9	690 ± 204	BVH	<27.9	<8	Y11
411	1	–17.35	23.0	98 ± 16	19.7 ± 0.8	35 ± 16	BH	<14.4		
450	1	–16.82	23.0	82 ± 14	20.9 ± 0.9	4.6 ± 2.8	BH	4.6		
462	2	–17.74	17.0	95 ± 11	21.9 ± 0.8	49 ± 15	BVH	<7.9	4.6 ± 0.4	Y11
482	2	–16.46	17.0	32 ± 22	14.6 ± 2.0	13 ± 4	BVH	<7.9		
486	2	–17.39	23.0	9.0 ± 7.6	21.6 ± 3.8	28 ± 10	BVH	<14.4		
498	–1	–12.76	17.0	20.8 ± 6.8	15.6[a]	0.13 ± 0.04	gi	<3.6		
571	1	–17.16	23.0	110 ± 27	16.1 ± 0.9	6.5 ± 4.1	BH	<14.4		
622	–1	–15.20	23.0	30.4 ± 11.1	15.6[a]	0.29 ± 0.08	gi	<6.6		
672	1	–17.69	23.0	60 ± 12	20.5 ± 1.0	20 ± 8	BVH	<14.4		
685	1	–19.28	17.0	25.8 ± 4.5	30.9 ± 2.1	237 ± 77	BVH	[e]	<1.5	Y11
705	–1	–14.04	17.0	30 ± 19	15.0 ± 2.0	0.55 ± 0.15	gi	<3.6		
710	–3	–16.41	17.0	64 ± 14	16.4 ± 0.8	1.4 ± 0.7	BVH	7.8		
758	1	–18.22	23.0	611 ± 61	22.1 ± 0.7	101 ± 30	BVH	8.7		
763	0	–21.07	17.0	20.0 ± 2.7[b]	29.0 ± 1.0	1309 ± 182	BVH	<7.9	<1.7	Y11
764	1	–16.33	17.0	30.4 ± 8.7	18.6 ± 1.1	4.9 ± 1.4	giH	6.8		
781	–3	–16.60	17.0	28.4 ± 9.4	18.4 ± 1.3	5.6 ± 2.3	BVH	<3.6		
788	–1	–15.49	17.0	17.5 ± 7.2	15.6[a]	1.3 ± 0.8	BH	<3.6		
832	–1	–12.30	17.0	19 ± 12	16.4 ± 2.1	0.26 ± 0.06	gi	<3.6		
881C	0	–21.22	17.0	29.7 ± 7.2	21.0 ± 1.2	1646 ± 422	BVH	8.9		
881SE				249 ± 56	13.9 ± 0.7				2.0 ± 0.2	D12
951	–2	–16.91	17.0	27.4 ± 6.8	20.0 ± 1.1	7.2 ± 2.7	BVH	<3.6		
1003	2	–20.14	17.0	228 ± 23	25.3 ± 0.9	682 ± 178	BVH	<7.9	11.2 ± 0.8	Y11
1030	1	–19.44	17.0	266 ± 28	23.9 ± 0.9	250 ± 83	BVH	<7.9	7.4 ± 0.7	Y11
1154	1	–19.98	17.0	189 ± 20	25.8 ± 1.0	413 ± 104	BVH	<7.9	17.4 ± 0.8	C07
1175	0	–15.92	23.0	7.1 ± 1.9	21.3[a]	1.8 ± 1.2	BH	<14.4		
1226	0	–21.94	17.0	31 ± 5	21.3[a]	2444 ± 658	BVH	<7.9	<1.8	Y11
1250	1	–18.37	17.0	120 ± 14	23.0 ± 0.9	45 ± 15	BVH	[d]	11 ± 1	Y02
1253	2	–19.98	17.0	57 ± 8	25.3 ± 1.1	353 ± 104	BVH	<7.9	3.5 ± 0.5	C07
1316	0	–21.67	17.0	21.9 ± 1.8[b]	21.3[a]	1725 ± 197	BVH	[d]	<1.5	C07
1327	0	–17.99	17.0	8.4 ± 1.5	21.3[a]	113 ± 22	BVH	[d]		
1420	–1	–14.87	17.0	50 ± 15	16.3 ± 1.2	1.2 ± 0.3	BVH	[d]		
1512	–3	–15.65	17.0	19.5 ± 4.9	17.6[a]	2.0 ± 1.2	BH	<3.6		
1535	1	–20.64	17.0	1096 ± 106	23.7 ± 0.8	877 ± 259	BVH	1.4	39 ± 1	C07
1578	–1	–11.57	17.0	27.4 ± 8.5	15.6[a]	0.015 ± 0.004	gi	<3.6		
1614	1	–16.91	17.0	8.6 ± 2.7	21.2[a]	8.8 ± 5.0	BH	<7.9		
1619	0	–18.82	17.0	25.5 ± 5.1	21.7 ± 1.0	106 ± 32	BVH	<7.9	1.6 ± 0.5	C07
1632	1	–20.55	17.0	8.4 ± 4.4[b]	21.2[a]	698 ± 196	BVH	<7.9	<1.9	C07
1684	–3	–16.41	17.0	10.8 ± 8.8	17.8 ± 2.9	2.2 ± 0.9	BVH	<3.6		
1706	–1	–11.35	17.0	13.8 ± 7.2	15.6[a]	0.041 ± 0.011	gi	<3.6		
1715	–1	–15.05	17.0	21.2 ± 8.1	15.6[a]	0.71 ± 0.46	BH	<3.6		

Notes. [(a)] The SED fit is done at fixed temperature. [(b)] The SED fit includes a synchrotron component. [(c)] Y02 = Young (2002); C07 = Combes et al. (2007); Y11 = Young et al. (2011); D12 = Dasyra et al. (2012). [(d)] This source could not be well observed by ALFALFA because of contamination from the M 87 radio continuum. [(e)] This source is outside the 4–16 deg declination strip observed by ALFALFA.

4.2. Stellar mass

Since stars are among the major dust producers, it is important to analyse the dust content in comparison with the stellar content, and we have estimated stellar masses for all the dust-detected ETG.

Stellar masses are estimated using broadband photometry in the optical range and, where available, in the near infrared (NIR), based on the synthetic libraries and the approach of Zibetti et al. (2009, hereafter ZCR09). The mass-to-light ratio M/L as a function of different colours or pairs of colours is obtained from the 50 000 models of the ZCR09 library, which are built based

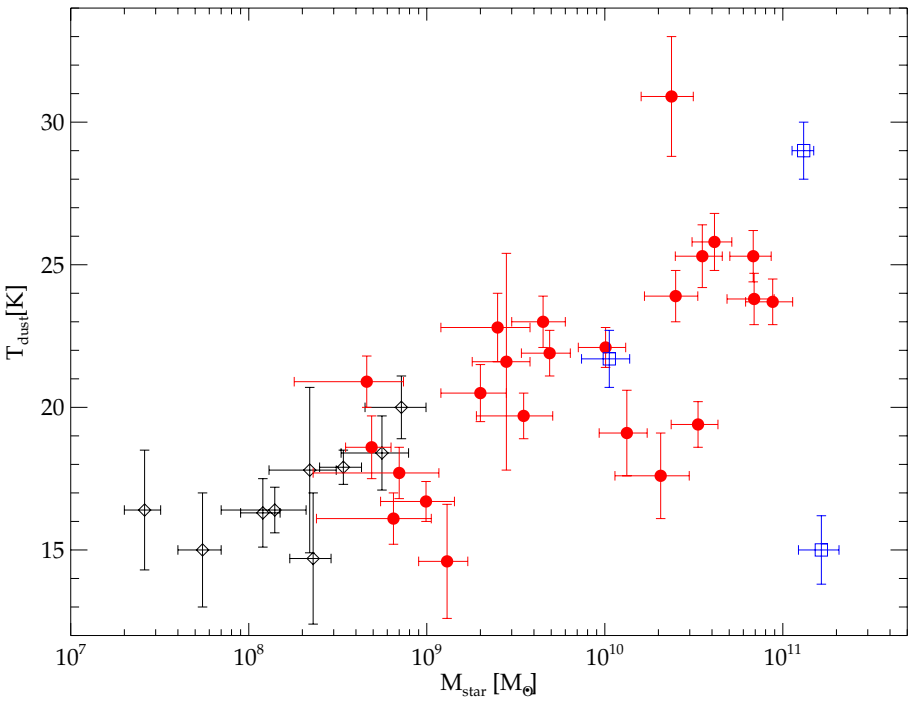

Fig. 3. Dust temperature as a function of the stellar mass, divided by morphological type. Open black diamonds are dwarf ETG, open blue squares are ellipticals and filled red circles are lenticulars. Only the 35 ETG with good modified black-body fits are displayed.

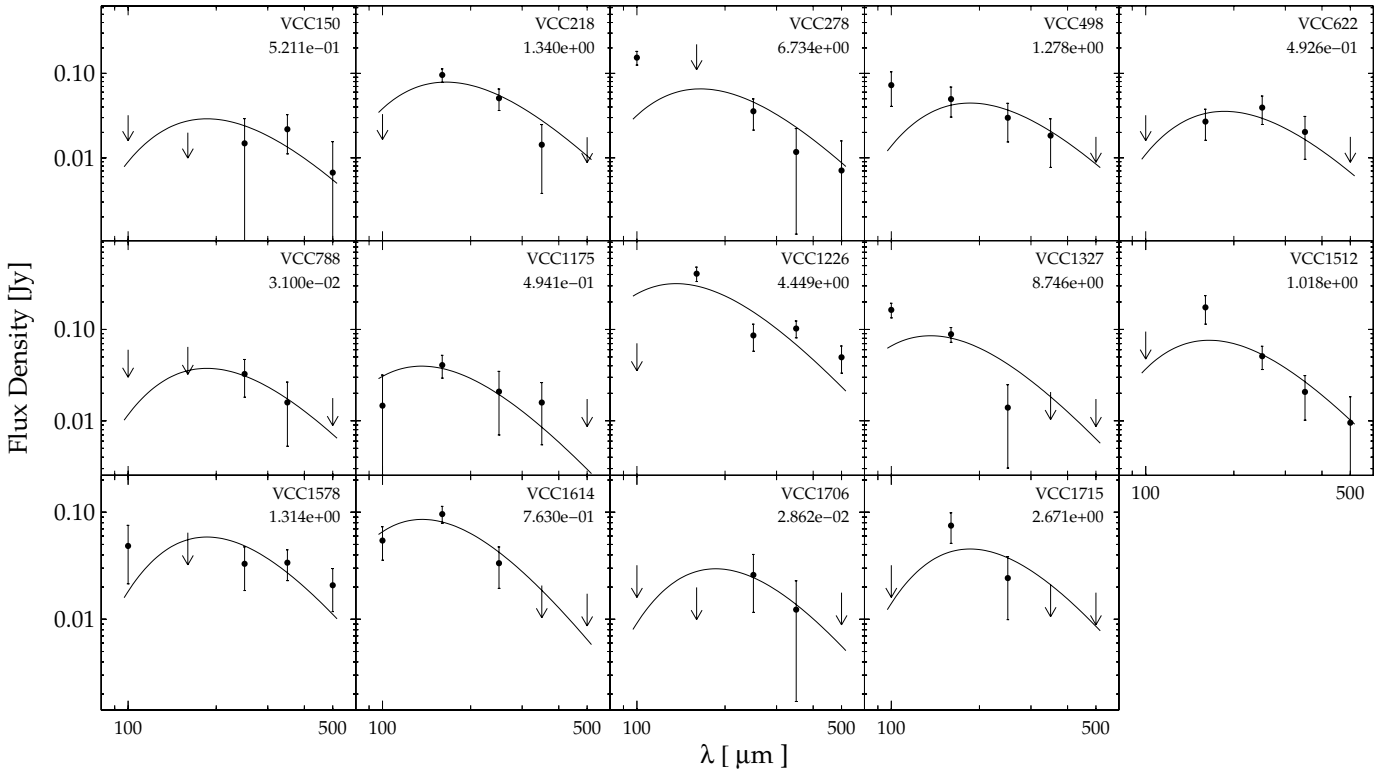

Fig. 4. Modified black-body fits to the HeViCS fluxes for the detected ETG fitted with a fixed temperature (see Table 4 for temperature value). The reduced χ^2 of each fit is listed under the object name. Upper limits to the fluxes are shown by downward arrows.

on the 2007 version of the Bruzual & Charlot (2003) models, assuming a Chabrier (2003) IMF.

Following ZCR09, the most reliable stellar mass estimates are obtained using a pair of one optical colour (e.g. $g - i$, $B - I$, $B - V$) and one optical-NIR colour (e.g. $i - H$, $V - H$) to compute M/L in a NIR band (e.g. H). We can apply this method to 30 galaxies in our sample. For 28 galaxies deep B-, V- and H-band photometry (BVH) is provided by the GOLDMine compilation, with total magnitudes determined from growth curves. Another 2 galaxies have GOLDMine H-band, but we have to rely on the SDSS photometry for the optical bands, namely g and i (giH in Table 4). In this case total GOLDMine magnitudes are combined with total "model" magnitudes of the SDSS, thus with larger systematic uncertainties due to a different extrapolation method. For the remaining galaxies only one colour is used to estimate M/L. Fourteen galaxies have

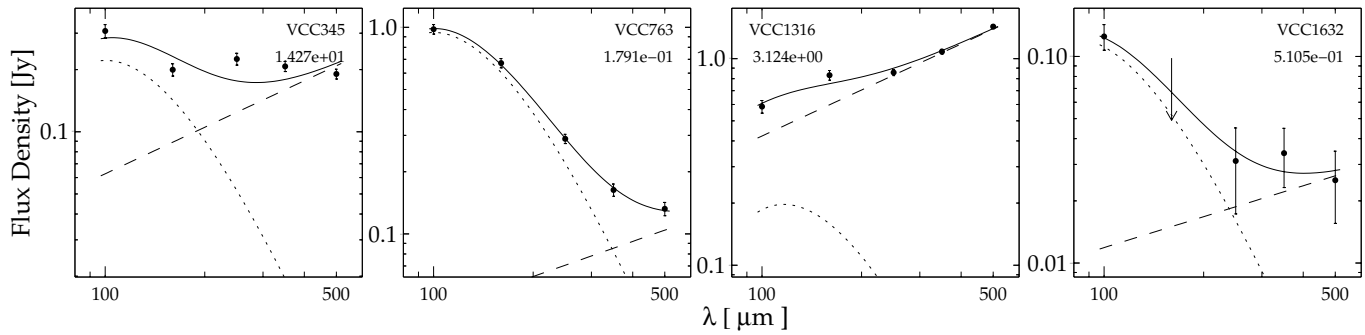

Fig. 5. Modified black-body fits to the HeViCS fluxes for the detected ETG with synchrotron emission. The synchrotron component is shown as a dashed line, the dust one as a dotted line. The reduced χ^2 of each fit is listed under the object name. Upper limits to the fluxes are shown by downward arrows.

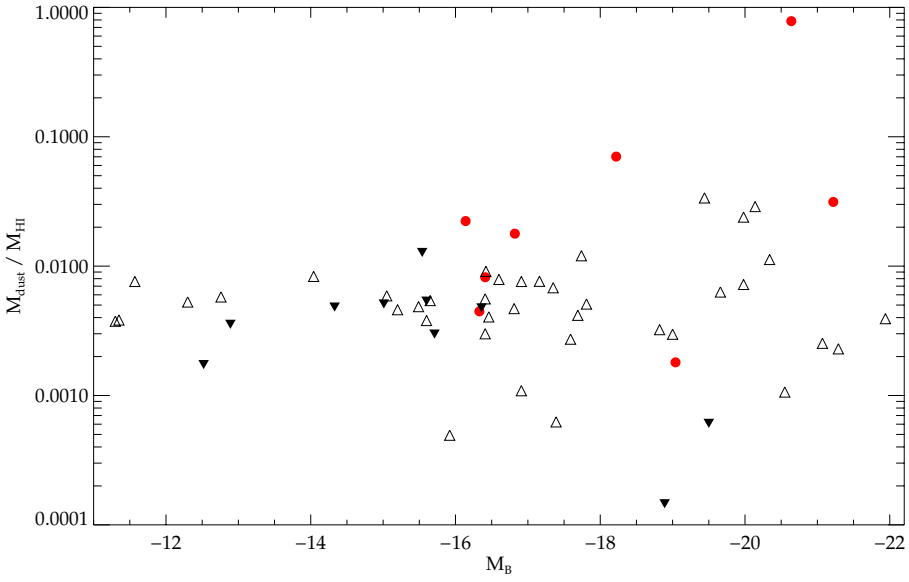

Fig. 6. Dust-to-gas mass ratio as a function of the absolute *B*-band magnitude for ETG in the Virgo cluster. Upward open black triangles are HI mass upper limits for dust-detected ETG, while downward filled black triangles are dust mass upper limits for HI-detected ETG.

deep *B*- and *H*-band photometry (*BH*) listed in GOLDMine: in this case the $B-H$ colour is used to estimate M/L in the *H*-band[2]. Another 8 galaxies do not have any photometry available from GOLDMine because of their low luminosity, so model magnitudes in *g* and *i* are extracted from the SDSS catalogs and stellar masses are computed based on the *i*-band luminosity (*gi* in Table 4). Although this combination of bands was shown to provide accurate results (ZCR09, Taylor et al. 2011) similar to the two-colour method, stellar masses for this subsample should be regarded as uncertain owing to the large photometric errors. All magnitudes are corrected for foreground Galactic extinction using the optical depth derived from Schlegel et al. (1998) and assuming the standard extinction laws of Cardelli et al. (1989) and O'Donnell (1994).

The stellar masses for the dust-detected ETG are listed in Col. 7 of Table 4, with errors accounting *only* for the intrinsic M/L scatter at fixed colour(s), as derived from the model library. While this is the largest contribution to the error budget for the brightest galaxies, fainter galaxies may indeed have much larger uncertainties because of photometric errors. The combination of bands used for the mass estimate is listed in Col. 8.

[2] The small bias introduced by the lack of a second optical band is corrected using the empirical correlation between $B-H$ and the difference in $\log M/L$ based on *BVH* and on *BH* only for the 28 galaxies where the three bands are available.

4.3. Other ISM components

Table 4 also contains complete information about the neutral atomic hydrogen (HI) content of the ETG detected in HeViCS. This information is obtained from the HI survey of ETG in the Virgo cluster done by di Serego Alighieri et al. (2007), using the Arecibo Legacy Fast ALFA (ALFALFA, Giovanelli et al. 2005, 2007). Appendix B of the present paper contains an update of that survey to extend it to the 4–8 deg, declination strip, which has recently become available in ALFALFA (Haynes et al. 2011). The result is that the HeViCS fields are now almost completely covered by the ALFALFA survey. Table 4 also contains the HI mass for VCC 450 and VCC 758, which have been detected in HI in the deeper Arecibo survey AGES (Taylor et al. 2012). The upper limits are described in di Serego Alighieri et al. (2007) for an assumed distance of 16.7 Mpc to the whole of the Virgo cluster, and are given in Table 4 for the distances assumed in this paper. Figure 6 shows the dust-to-atomic-gas mass ratio for Virgo ETG, showing large variations, even for objects with the same luminosity.

We also give in Table 4 the information about the molecular gas (H_2) content which is available in the literature. This information, contrary to that for dust and HI, is far from complete for the ETG of our input catalogue. The only ETG in our sample that has been detected both in atomic and molecular gas, i.e. the S0 galaxy VCC 1535 (NGC 4526), has a high

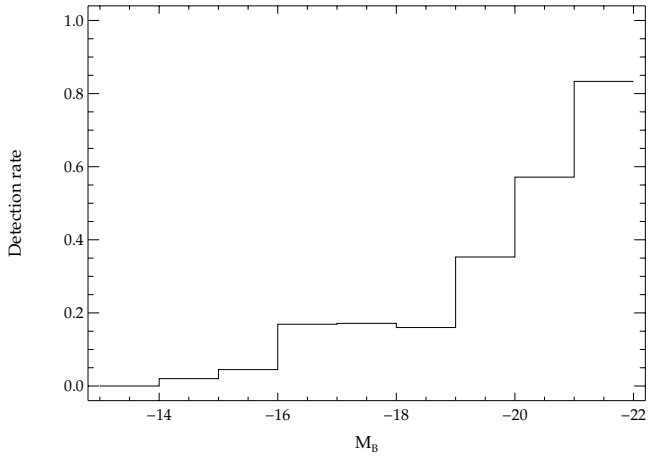

Fig. 7. Dependence of the dust detection rate on the optical luminosity for our complete samples.

molecular-to-atomic-gas mass ratio ($M_{H_2}/M_{HI} = 28$), consistent with the trend to higher values in this ratio for earlier spirals (Young & Scoville 1991), but considerably higher than the values reported by Welch et al. (2010) for about a dozen elliptical and lenticular galaxies. In summary only one ETG in our sample (VCC 1535) has been detected in HI, H_2, and dust, while 8 ETG have been detected in both HI and dust, and 9 ETG in H_2 and dust. For these 9 galaxies the dust-to-molecular-gas mass ratios are all between 1×10^{-2} and 4×10^{-2}, and the lower limits to this ratio are consistent with this range.

5. Discussion

5.1. Dust detection rates

Since detection rates are meaningful only on complete samples, we examine detection rates only for the 43 galaxies detected above the FIR completeness limit ($F_{250} \geq 25.4$ mJy), and in the optically complete input sample ($m_{pg} \leq 18.0$). For the dwarf ETG (GOLDMine types = −3, −2, −1) we detect 13 galaxies out of 354 (3.7%); for the ellipticals (GOLDMine type = 0) we detect 6 out of 35 galaxies (17.1%); and for the lenticulars (GOLDMine types = 1 and 2) we detect 24 galaxies out of 58 (41.4%). The detection rates for ellipticals and lenticulars are lower than the corresponding rates obtained for the Virgo part of HRS sample by Smith et al. (2012) which are 29% and 53%, respectively, and are also lower than those obtained by Knapp et al. (1989) with IRAS and by Temi et al. (2004) with ISO. The reason for our lower detection rates is probably because our input sample includes fainter objects, and the detection rate increases with the optical luminosity, as shown in Fig. 7. On the observational side, the dependence of the detection rate on optical luminosity could be related to our dust detection limits, which favour more luminous galaxies. On the other hand, it might also be related to the difficulties that dwarf galaxies have in retaining their dust, particularly if the dust-to-star mass ratio reaches such high values to see the onset of massive star formation, which would lead to SN feedback and to a fast depletion of the ISM.

There are two remarks about our detection rates, however. The first is due to the fact that our complete input sample, which we selected to avoid galaxies with $V_{hel} > 3000$ km s^{-1}, actually includes 102 ETG for which the radial velocity is not known (these are all dwarf ETG). Potentially, some of these can have a radial velocity larger than 3000 km s^{-1}. They would then be background galaxies not belonging to the Virgo cluster and should be excluded from our input sample[3]. By assuming that the probability for a galaxy to be a background contaminant is independent of whether a measured radial velocity is available or not, the fraction of contaminants among VCC galaxies without a valid radial velocity measurement is the same as among VCC galaxies with available radial velocity, i.e. 7.8%. Hence, only 8 of the 102 ETG without a measure of V_{hel} in the optically complete sample are expected to be background contaminants, and should therefore be excluded from the complete input sample. Assuming that these background galaxies are among those not detected in dust (in fact only two ETG of the complete detected sample for the optically complete input sample have no measured radial velocity), then the dust detection rate for dwarf ETG becomes 3.8% (13 out of 354–8 = 346).

The second remark is that in Sect. 3.2 we examined the probability that some of our FIR counterparts are actually associated with background galaxies, whose position coincides with that of a Virgo ETG of our input sample, and concluded that these could be 4–8 dwarf galaxies misidentifications, and 0–4 lenticular ones. In this case then, the dust detection rate for dwarf Virgo ETG would be reduced to between 2.6% and 3.2%, and the rate for lenticular galaxies to between 38% and 41%. The dust detection rates for the brighter ETG have not changed, since all of them have a measured radial velocity, and are not likely to be confused with background sources.

5.2. Dust vs. stars

Dust could originate from stellar/SN mass loss within each galaxy, or it could have an external origin. If the former were true, we should see a dependence of the dust mass on the stellar mass, at least within each morphological type, assuming similar star-formation histories and similar efficiencies for the processes of dust destruction, depletion and loss. Figure 8 shows the comparison between dust mass and stellar mass. There is no clear dependence, particularly if one takes into account that the lower part of the figure is empty because of the dust detection limits, which vary between 5 and 18 $\times10^4$ $M_\odot$ at 17 Mpc, and are larger at greater distances (see Sect. 4.1). Young et al. (2011) also found no dependence of the molecular gas content of Virgo ETG with their mass. The dust-detected ETG span about 6 orders of magnitude in stellar mass, but only 2.5 orders of magnitude in dust mass.

We now examine the idea that the dust produced locally in a passive galaxy can account for the observed dust content. Assuming that an ETG was already in place at $z = 1$ and its stellar population has passively evolved since $z = 10$ as a closed-box single-stellar-population model (Solar metallicity, Salpeter IMF for 0.1–120 $M_\odot$, Pierini et al. 2004), about 10% of its mass was returned by stellar mass loss since $z = 1$. The dust mass associated with these stellar outflows that survives today should at most give a dust-to-star mass ratio of

$$\frac{M_{dust}}{M_{star}} \leq \frac{1}{9} * \frac{M_{dust}}{M_{HI}} * \frac{t_{surv}}{t_{z=1}} = 0.11 * \frac{1}{150} * \frac{7.1\times10^7}{7.7\times10^9} = 6.8\times10^{-6}, \quad (3)$$

where for the dust-to-neutral-gas mass ratio we have used the Galactic value, and for the dust grain survival time we have used the constraint $t_{surv} < 46 + 25$ Myr, the maximum allowed by

[3] However, Binggeli et al. (1985) have classified, based on their visual inspection, all of these 102 ETG without radial velocity either as cluster members (95) or as possible members (7).

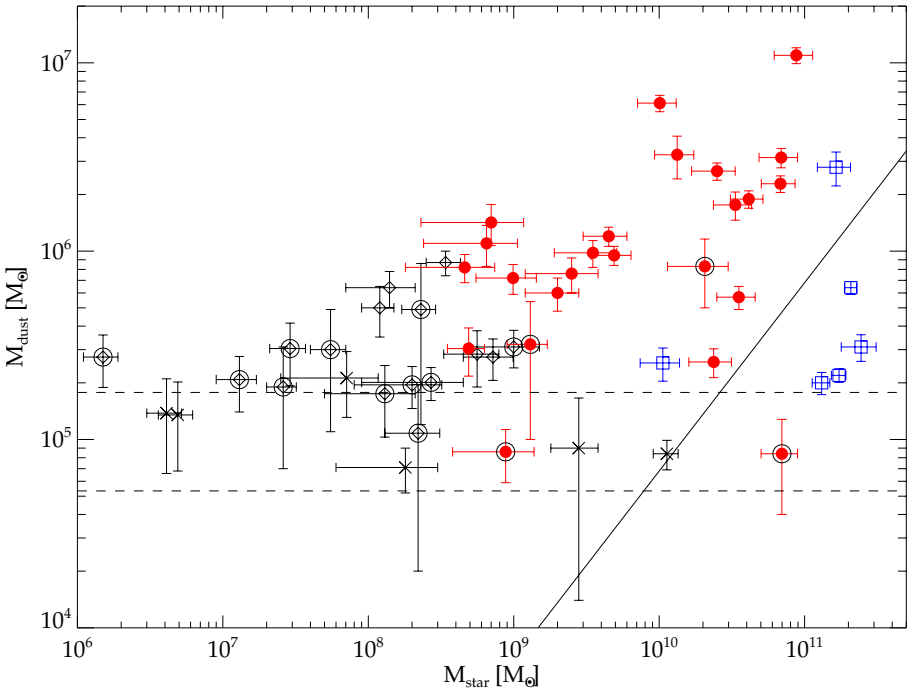

Fig. 8. Dust mass as a function of the stellar mass, divided by morphological type. Open black diamonds are dwarf ETG, open blue squares are ellipticals and filled red circles are lenticulars. Black crosses are objects which have a 250-μm flux below the limit of 25.4 mJy. Objects with a black circle are in the two lowest flux bins of Table 3: half of them are probably contaminating background galaxies. The continuous line shows the dust mass upper limit for the closed-box passively-evolving model (Eq. (3)). The dotted lines show the range of the dust mass detection limit for a distance of 17 Mpc (Eq. (2)).

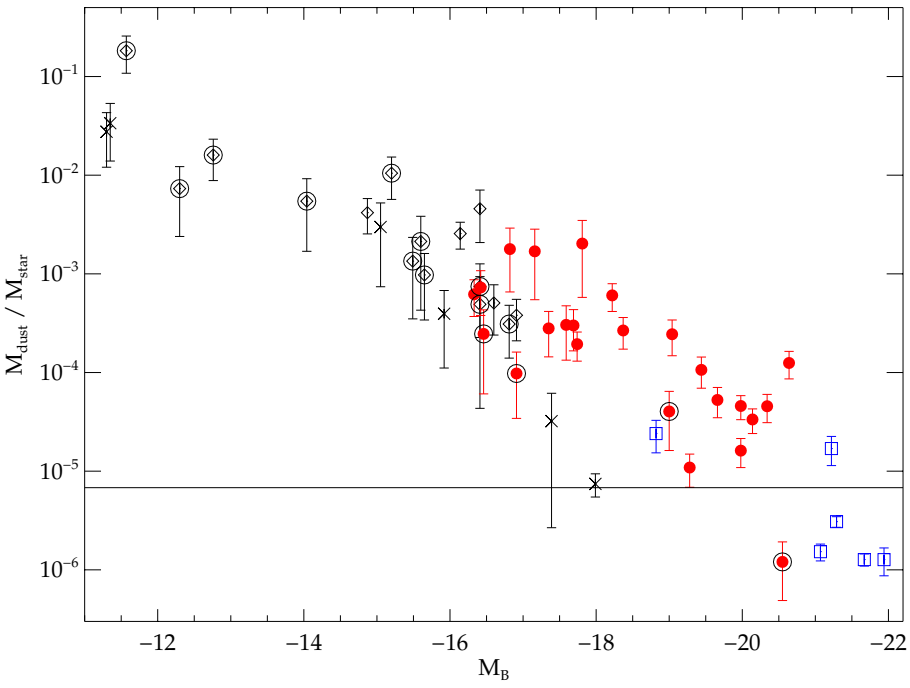

Fig. 9. Dust-to-star mass ratio as a function of *B*-band luminosity divided by morphological type. Symbols are as in Fig. 8. The continuous line shows the upper limit for the closed-box passively-evolving model (Eq. (3)).

Clemens et al. (2010) for a passive galaxy. The constraint given above on the dust-to-star mass ratio is satisfied by our observations of the Virgo ETG sample only for a few very massive ETG (see Figs. 8 and 9). On the other hand, it is based on rough numbers and simple assumptions. Large discrepancies from analogous values obtained from the previous equation along the mass range should be understood as differences in the origin of dust (in general: ISM, outflows from SN Type II/OB associations, and dust cycle in diffuse media, or dust of external origin) or higher values of dust-to-neutral-gas mass ratio or of the dust grain survival time, for instance.

Looking at the dust-to-stars mass ratio shown in Fig. 9, there is a clear tendency of this quantity to decrease with luminosity for the dust-detected ETG, an effect which cannot be totally due to our incompletenesses. The observational limits on the dust detection can account for the lack of objects in the lower left of the figure, but not in the upper right. While ellipticals and S0 have dust-to-star mass ratios between 10^{-6} and 10^{-3}, this ratio can raise to about half a percent for dwarf ETG (excluding higher values obtained for objects possibly contaminated by background galaxies), as much as for the dusty late-type galaxies (Cortese et al. 2012). Interestingly, the lenticular galaxies span a range of dust-to-star mass ratio which goes to substantially larger values than the HRS sample (Cortese et al. 2012; Smith et al. 2012). This is due to the presence of fainter galaxies of this type in our sample.

Figure 3 shows that the dust temperature correlates with the stellar mass of the galaxy. ETG with stellar masses up to 10^9 $M_\odot$

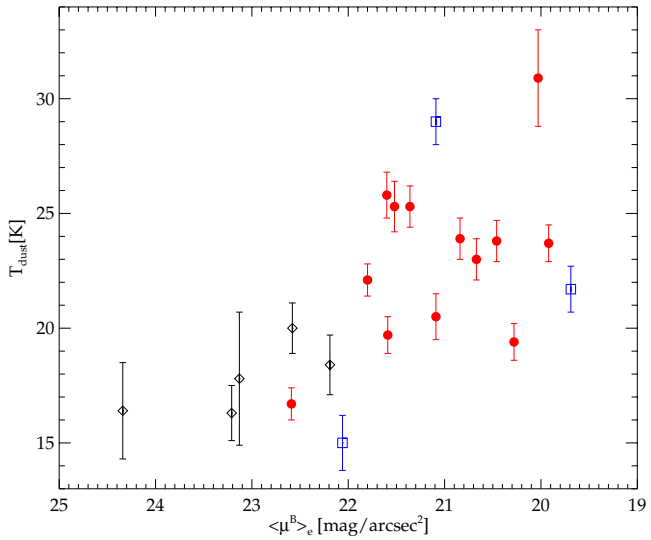

Fig. 10. Correlation between the dust temperature and the *B*-band average surface brightness within the effective radius for the object for which this radius is available. Open black diamonds are dwarf ETG, open blue squares are ellipticals and filled red circles are lenticulars.

exhibit cold dust temperatures ($T_{dust} \lesssim 20$ K in agreement with values that are typical of the diffuse interstellar medium in star-forming galaxies. On the other hand, temperatures tend to be higher in more massive ETG. The latter galaxies might have an increased contribution to the emission at the PACS wavelengths from circumstellar dust or from stochastic heating, or a more intense interstellar radiation field, associated with post-main-sequence phases of the evolution of super-solar metallicity low-intermediate-mass stars or, alternatively, recent star formation activity (e.g. Kaviraj et al. 2007). The higher dust temperature in more massive galaxies could also be due to conductive heat transfer from the X-ray gas (Sparks et al. 2012, and references therein). Figure 10 shows that the dust temperature also correlates with the *B*-band average surface brightness within the effective radius, as listed in GOLDMine, indicating clearly a higher dust heating in objects with a stronger radiation field.

We find that dust is much more concentrated than stars. In most of the dust-detected ETG the FIR counterpart is broadly consistent with a point source at 250 μm. The few clearly extended counterparts are for the 12 galaxies for which we had to use a photometric aperture larger than 30 arcsec, as listed in Table 1 and shown in Fig. 1, but also in these cases the dust tends to be much more concentrated than stars.

The ATLAS^{3D} collaboration (Cappellari et al. 2011)[4] convincingly argues that the most important distinction among (bright) ETG is between slow and fast rotators (Emsellem et al. 2011). Therefore, although most of the ETG of our input sample lack the detailed kinematic information necessary for this distinction, we have looked at the relationship between the presence of dust and the stellar kinematics for those objects where this is possible. We note that among the 50 ETG that are in common between our input sample and the ATLAS^{3D} sample (and therefore have accurate kinematics), 13 are classified as slow rotators within one effective radius, and 37 are classified as fast rotators (Emsellem et al. 2011). Since we detect dust above the completeness limit of 25.4 mJy at 250 μm in 9 slow rotators (69 ± 23%) and in 9 fast rotators (24 ± 8%)[5], it appears that the slow rotators, although less abundant in a cluster, are much more likely to contain dust. This result surprisingly contrasts the tendency for molecular gas to be found preferentially in fast rotators: Young et al. (2011) in the ATLAS^{3D} sample find that the CO detection rate is 6 ± 4% among slow rotators and 24 ± 3% among fast ones.

This difference suggests that the relationship between molecular gas and dust on the one hand, and kinematics on the other hand might depend strongly on the environment, being different in the Virgo cluster and for field galaxies. Most of the ATLAS^{3D} galaxies, i.e. those for which Young et al. (2011) obtained their results on the molecular gas, are outside Virgo. In addition, if one takes only the 50 ETG that we have in common with ATLAS^{3D}, molecular gas is detected in 23% of the slow rotators (3 out of 13) and in 14% of the fast ones (5 out of 37), with slow rotators more efficiently detected, similar to the rates we find for the dust detections, and contrary to the molecular gas detection rates found in the whole ATLAS^{3D} sample, which is mostly made of field objects. However, the difference could be caused by the presence of kinematically peculiar objects among the dusty slow rotators in the Virgo cluster, such as galaxies with counter-rotating components mimicking slow rotation. Nevetheless this possibility can be excluded, since the brightest ellipticals and lenticulars in the Virgo cluster like M 49, M 84, M 86, M 87, M 89, NGC 4261 and NGC 4552 are among the dusty slow rotators, and only one dusty slow rotator (NGC 4550) has counter-rotating components. This strengthens our suggestion that the ETG most likely to contain dust and molecular gas are slow rotators in the Virgo cluster and fast rotators in the field. Davis et al. (2011) find that the gas has a purely internal origin (and a smaller amount) in fast rotators residing in dense environments, while it has an external origin, possibly leading to larger amounts, in about half of the fast rotators in the field. They also find that the dominant source of gas is external for slow rotators, which are mainly found in dense enviroments. We tentatively conclude that the cluster environment might favour cold ISM accretion from other galaxies particularly for slow rotators, which appear to be more concentrated in the densest parts of the cluster than fast rotators.

5.3. Dust vs. gas and spatial distributions

Although dust detection rates and atomic-gas detection rates (see di Serego Alighieri et al. 2007, and Appendix B) are similar for the Virgo ETG, and the dust-to-gas mass ratios which we obtain are similar to those obtained by Cortese et al. (2012), the comparison between Table 4 and Table B.1 in Appendix B (see also Fig. 6) shows that there is a surprisingly small overlap between dust-detected and atomic-gas-detected ETG: there are only 8 ETG detected both in dust and in atomic gas, while there are 39 ETG detected in dust, but not in atomic gas, and 8 ETG detected in atomic gas, but not in dust. This comparison has a strong observational basis, given the completeness of both the atomic gas and the dust surveys for Virgo ETG.

An additional important clue to this incompatibility between dust and atomic gas in Virgo ETG is given by their respective location in the cluster. Figure 11 illustrates the spatial distribution in the Virgo cluster of all the ETG examined in this work and of those for which dust and HI have been detected (see Appendix B). These spatial distributions show several

[4] ATLAS^{3D} is a project for obtaining two-dimensional kinematics for a volume-limited sample of 260 bright ETG ($D < 42$ Mpc, $M_K < -21.5$).

[5] Two additional slow rotators (IC 782 and NGC 4486A) are detected below the completeness limit (see Table 2), but are not used in these statistics.

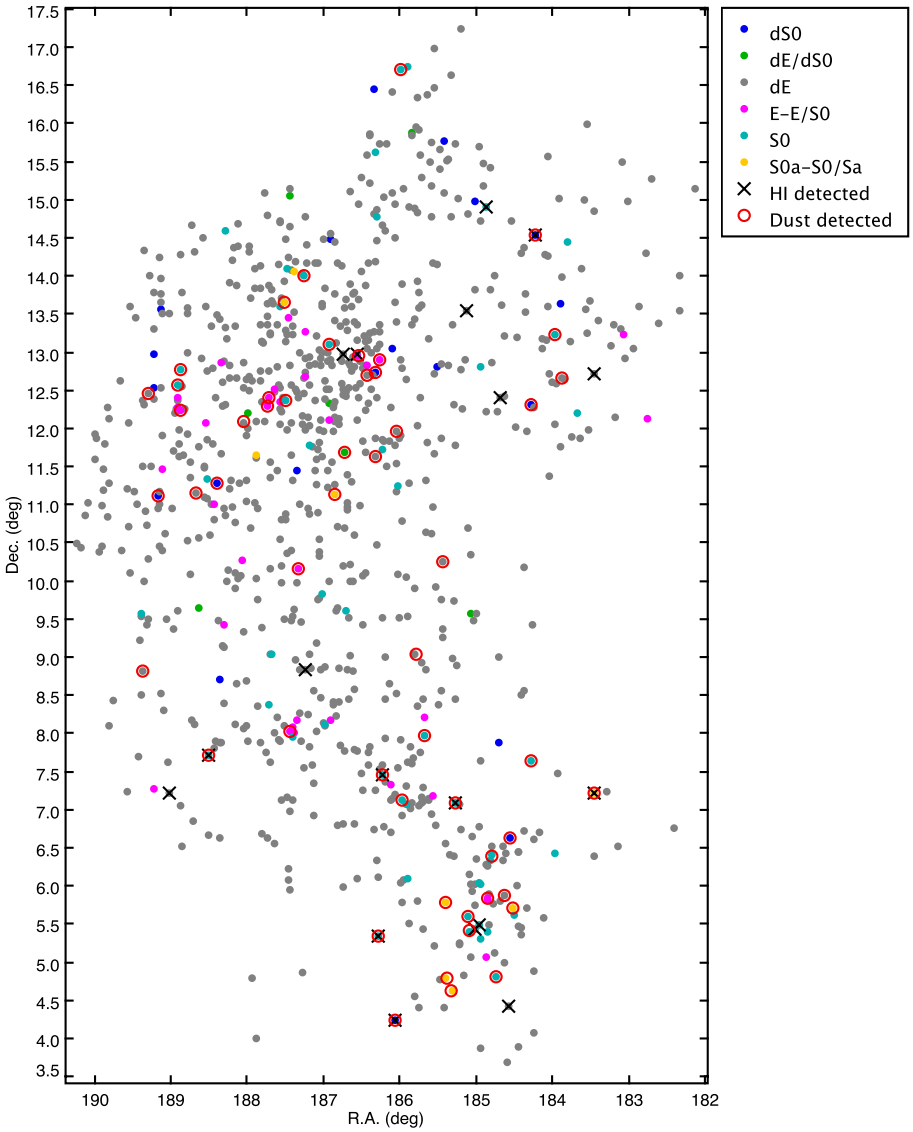

Fig. 11. Map of all the ETG examined in HeViCS, distinguished by morphological type. Those marked with a red circle have been detected in dust, while those marked with a black X have been detected in HI.

interesting features. First, the dust-detected ETG tend to concentrate at the centre of the main clouds in the Virgo cluster, i.e. the central cloud A around M 87, cloud W to the south-west, and cloud M to the west, while, as noticed by di Serego Alighieri et al. (2007), the HI-detected ETG tend to be at the periphery of the cluster. This fact remains true even considering the HI-blind region within one degree from M 87. We suggest that this is because atomic gas is more affected than dust by the hot gas, which tends to concentrate on the densest regions of the cluster. This would have implications on the star-formation rate of cluster ETG, in particular if, as we suspect, the distribution of molecular gas is more similar to that of the dust than to that of atomic gas. The tendency of dust-detected ETG to concentrate on the cluster clouds is reinforced by the fact that 15 out of the 25 lenticular galaxies present in the south-west part of the cluster (RA < 186.5 deg and Dec < 8.0 deg, cloud W) are detected in dust, with a detection rate of 60%, considerably higher than the lenticular detection rate of 41% obtained on average for the Virgo cluster. The evidence that dust may not be, at least in some cases, much affected by the diffuse hot gas might lead to a revision of our estimates about dust survival in passive ETG (Clemens et al. 2010).

Another mechanism which could produce the "incompatibility" between dust and atomic gas observed in Virgo ETG is the recombination of molecular hydrogen on the surface of cold dust grains (Hollenbach & Salpeter 1971). If so, where dust is present, atomic hydrogen could recombine in molecules; the result is less atomic gas and more molecular gas in the dusty ETG. In fact in the only dust-detected ETG (VCC 1535), for which we have the mass of both the molecular hydrogen and the atomic hydrogen, their ratio is high ($M_{H_2}/M_{HI} \sim 30$), and there are several lower limits around 1 for this ratio in other ETG with dust. Nevertheless, dust favours recombination only locally, and this effect could not explain the lack of atomic hydrogen at great distances from the galaxy centre, since dust appears to be very concentrated in ETG. In the outer parts of galaxies the lack of hydrogen is probably caused by ram pressure stripping, which is quite effective on diffuse atomic gas, but not so effective on dust, particularly if it is concetrated and clumpy, owing to self shielding (see Cortese et al. 2010 for evidence that dust and gas can both be stripped in late-type Virgo galaxies).

In summary, the presence in the Virgo cluster of several ETG with dust, but with only an upper limit to the HI mass, can be explained by the different gas and dust survival times, by the stronger effects of ram pressure stripping on neutral atomic gas than on dust, and by the recombination of H_2 on grains. We are surprised, however, by the ETG for which HI has been detected but for which there is only an upper limit to the dust

mass (see Fig. 6). Among these, two are bright S0 galaxies with $M_B \simeq -19$: NGC 4262 and NGC 4270. The lack of dust in these objects could be explained by low metallicity, according to the relationship between the gas-to-dust mass ratio and the metallicity proposed by Draine et al. (2007). However, the metallicity of these two galaxies, although slightly below solar (Kuntschner et al. 2010), is not as low as the Draine relation would require to explain the observed upper limit on the dust-to-gas mass ratio. Both of these galaxies have been observed in CO by Combes et al. (2007), but have not been detected. We cannot exclude that some of these galaxies detected in HI but not in dust might actually have dust emission whose peak does not coincide with the optical centre and, therefore, would be undetected by our procedure, which relies on the precise superposition of the optical and FIR peaks. This actually happens in the case of M 87 (VCC881) and has been noticed, also thanks to the overlap of the dust emission with an Hα filament. A similar procedure might also help to solve some of the other cases.

6. Conclusions

We have searched for dust in an optically-selected sample of 910 ETG in the Virgo cluster, 447 of which are complete to $m_{pg} \leq 18.0$, using the FIR images of HeViCS at 100, 160, 250, 350, and 500 μm, which cover a large fraction of the cluster.

From this study we obtain the following results:

1. We detect dust above the detection limit of 25.4 mJy at 250 μm in 46 ETG, 43 of which are in the optically complete part of the input sample. In addition, we detect dust at fainter levels in another 6 ETG. In all cases dust has been detected in more than one band.
2. We detect dust in the 4 ETG with synchrotron emission, including M 87.
3. Considering only the complete detections ($F_{250} \geq 25.4$ mJy) out of the optically complete input sample, dust detection rates are 17.1% for ellipticals, between 37.9% and 41.4% for lenticulars (S0 + S0a) and between 2.6% and 3.2% for dwarf ETG, depending on the effects of background galaxies.
4. Dust appears to be much more concentrated than stars.
5. We estimate dust masses and temperatures with modified black-body fits. Dust masses range between 7×10^4 and 1.1×10^7 $M_\odot$, and temperatures between 14 and 31 K, with higher temperatures for more massive galaxies.
6. The dust mass does not correlate clearly with the stellar mass, and is often much greater than expected in a closed-box passively-evolving model, suggesting a possible external origin.
7. In the Virgo cluster slowly rotating ETG appear more likely to contain dust than fast rotating ETG, contrary to what is observed for the molecular gas content for field galaxies, suggesting an environmental effect on the dust and molecular gas content in slow and fast rotators.
8. Comparing the dust results with those on HI from ALFALFA, there are only 8 ETG detected both in dust and in HI, while 39 have dust but no HI, and 8 have HI but no dust. Locations are also different, with the dusty ETG concentrated in the densest regions of the cluster, while the HI rich ETG are at the periphery.

We conclude that, while general dust detection rates for ETG are smaller than for later galaxy types, the dust-to-stellar mass ratio for some dwarf ETG is comparable to that of most dusty late-type galaxies. We suggest that at least in some cases the dust has an external origin in cluster ETG, and that the dust survives in ETG much longer than the neutral atomic gas.

Acknowledgements. We thank everyone involved with the *Herschel* Space Observatory and with SPIRE and PACS. We thank Laura Ferrarese and Thorsten Lisker for useful information on the Virgo cluster galaxies and Bruce Draine for useful comments and advice. S.diS.A., S.B., E.C., G.G., C.G., L.K.H., L.M., and C.P. are supported through the ASI-INAF agreements I/016/07/0 and I/009/10/0. C.P. is also supported by the PRIN-INAF 2009/11 grant. M.G. gratefully acknowledges support from the Science and Technology Foundation (FCT, Portugal) through the research grant PTDC/CTE-AST/111140/2009.

Appendix A: Revised coordinates for a subsample of the VCC

The coordinates for the VCC objects used in this work were originally extracted from NED. For most objects more than two positions are available from the literature, and the coordinate accuracy quoted in NED is $\leq 1''$. However, for 476 VCC objects (both inside and outside the HeViCS fields), NED provides only the coordinates from the original work by Binggeli et al. (1985) (as of September 2012); for these objects, NED quotes a positional accuracy of $25''$ in both coordinates, which is inadequate for our work. Indeed, a visual check on SDSS7 images clearly showed that this inaccuracy of the position could result in an incorrect match with HeViCS sources.

Thus, we revised the coordinates by using SDSS7 r-band images, which are deeper and better suited to detect dwarf ETG. Thumbnail images of $3'\times3'$ around the original coordinates were produced; the images were smoothed, and contours overplotted as a guide to the eye; the object centre was then flound manually by selecting a position on the image. For the fainter objects, we cross-checked the identification of the source by using DSS-2 images and GOLDmine images, when available. In the selection of the object which corresponds to the VCC galaxy, we were guided by the photographic magnitude m_{pg} and the dimensions indicated in the VCC catalogue.

We have been able to identify 454 objects, whose revised coordinates are given in Table A.1. For the remaining 22 VCC entries, instead, no unequivocal position could be found because there was more than one suitable candidate object for a given position, or no identifiable object at all. These VCC galaxies are: VCC 203, 445*, 463*, 474*, 487*, 553*, 835, 852*, 910*, 913*, 927*, 969*, 987*, 1116*, 1181, 1241*, 1260*, 1315, 1350*, 1571, 1835, 2079 (those with an asterisk are ETG in the HeViCS fields, and are therefore part of the input sample for this paper). Unsurprisingly, most of them are dE with $m_{pg} > 19.0$. One notable exception is VCC 1571, whose position lies within $20''$ of a relatively large ($\approx30''\times45''$) and bright ($m_{pg} = 16.0$) dE, VCC 1570, and is listed with very similar properties to those of its neighbour; this appears to be a duplicate entry in VCC.

In Fig. A.1 we show the offsets along RA and Dec. between the original VCC positions and the revised positions (red symbols). The red circle, which contains the offsets for 68% of the objects, has a radius $\Delta r = 10''$. Assuming a Gaussian distribution of the offsets, this radius corresponds to the standard deviation. It corresponds to the coordinate accuracy quoted by Binggeli et al. (1985). While for most of the objects $\Delta r \lesssim 25''$ (the *NED accuracy*), for a few of the objects (20) the offset is larger than that. The largest offset is for VCC171, a relatively bright and large Im galaxy ($m_{pg} = 17.4$, size $\sim35\times20'$) which, thanks to the illustrated atlas of Sandage & Binggeli (1984) (where the galaxy is called 8°7), is identified with an object at $\Delta r = 3.25''$ from the original coordinates (beyond our original thumbnails). Besides this galaxy, all other identified galaxies

Table B.1. Virgo ETG detected in HI in the α.40 catalogue ($4° < \mathrm{Dec} < 16°$).

ID	Other name	m_{pg}	Type GM[1]	Type VCC/NED	$cz_{opt.}$ km s^{-1}	cz_{HI} km s^{-1}	D Mpc	M_{HI} 10^7 $M_\odot$	M_B	log (M_{HI}/L_B) $M_\odot/L_\odot$
CGCG69043	NGC 4078	13.9	1	S0?	2592	2572	17.0	4.8	–17.37	–1.46
VCC 21	IC 3025	14.75	–3	dS0(4)	506	485	17.0	5.9	–16.49	–1.02
VCC 93	IC 3052	16.3	–1	dE2	910	841	32.0	13.3	–16.36	–0.61
VCC 94	NGC 4191	13.57	2	S0/a		2659	32.0	180.2	–19.04	–0.55
VCC 180		15.3	1	S0 pec	2232	2239	32.0	6.5	–17.32	–1.31
VCC 190		18.0	–1	dE4		2352	32.0	13.8	–14.63	0.09
VCC 209	IC 3096	15.15	–3	dS0?	1208	1263	17.0	3.9	–16.14	–1.06
VCC 282		17.0	–1	dE5?	2014	1985	32.0	11.8	–15.60	–0.36
VCC 304		16.3	–1	dE1 pec?	155	132	17.0	3.5	–15.01	–0.66
VCC 355	NGC 4262	12.41	1	SB0	1359	1367	17.0	58.9	–18.89	–0.98
VCC 375	NGC 4270	13.11	1	$S0_1(6)$		2377	32.0	49.9	–19.50	–1.30
VCC 390		16.9	–1	dE3	2479	2474	32.0	21.2	–15.71	–0.15
VCC 421		17.0	–1	dE2		2098	17.0	3.7	–14.33	–0.36
VCC 710		14.9	–3	dS0:	1175	1182	17.0	7.8	–16.41	–0.86
VCC 764		14.83	1	$S0_2(6)$	2044	2020	17.0	6.8	–16.33	–0.89
VCC 881	NGC 4406	10.06	0	$S0_1(3)$/E3	–244	–302	17.0	8.9	–21.22	–2.73
VCC 956		18.75	–1	dE1,N:		2151	17.0	10.3	–12.52	0.81
VCC 1142		19.0	–1	dE		1306	23.0	9.2	–12.89	0.62
VCC 1391		18.5	–1	dE		2308	17.0	2.6	–12.75	0.12
VCC 1533		18.0	–1	dE2,N		648	17.0	2.9	–13.25	–0.02
VCC 1535	NGC 4526	10.61	1	$S0_3(6)$	448	560	17.0	1.4	–20.64	–3.31
VCC 1617		15.0	–3	d:S0(4) pec?		1600	17.0	3.8	–16.25	–1.11
VCC 1649		15.7	–1	dE3,N:	1038	972	17.0	1.4	–15.54	–1.28
VCC 1993		15.3	0	E0	875	925	17.0	5.0	–15.96	–0.88
VCC 2062		19.0	–1	dE:	1146	1141	17.0	38.5	–12.32	1.46
CGCG100011	NGC 4710	11.6	2	SA(r)0+? sp	1129	1100	17.0	5.7	–19.68	–2.31

Notes. GOLDMine type: –3=dS0 –2=dE/dS0 –1=dE(d:E) 0=E-E/S0 1=S0 2=S0a-S0/Sa.

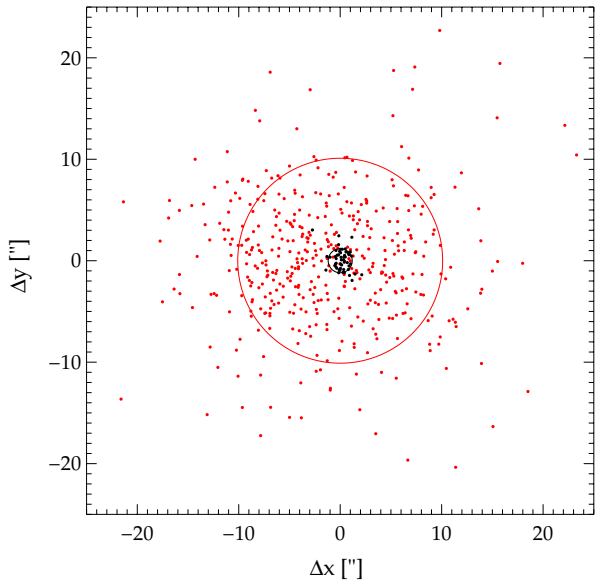

Fig. A.1. Offsets along R.A. and Dec. between the original coordinates and those of Table A.1 (red points). The red circle ($\Delta r = 10''$) contains 68% of the sample considered here. Black dots and circle ($\Delta r = 1.2''$) show the offsets between the Lisker's coordinates (priv. comm.) and our values.

have $\Delta r \leq 67.5''$ (the value for VCC 709). Offsets from VCC coordinates, along with m_{pg} and the GOLDMine morphological type, are given in Table A.1.

Lisker et al. (2007) derived accurate coordinates for the Virgo cluster early-type dwarf galaxies with $m_{pg} \leq 18$, by minimising the object's asymmetry within a Petrosian aperture on SDSS5 images. For 53 of these objects, which are in common with those listed in Table A.1, we show the offsets between the coordinates obtained by Lisker (priv. comm.) and those derived here (blue symbols) in Fig. A.1. Despite our *rough* manual technique, 68% of our coordinates are within 1″ (blue circle) of those obtained by Lisker et al. (2007), and all of them within 4″.

The offsets between the improved positions and the original positions by Binggeli et al. (1985) are very similar for our full set of 454 galaxies as for the 53 objects which we have in common with Lisker. Thus, we believe that our position accuracy is within a few arcsec, also for the fainter galaxies ($m_{pg} > 18$). We make this table available to the community as a valuable dataset, while waiting for the deeper imaging and more accurate positions which will be derived for the Next Generation Virgo Cluster Survey (NGVS, Ferrarese et al. 2012).

Appendix B: The Virgo ETG detected in HI with ALFALFA

For a proper study of the cold ISM in ETG it is important to have information on the neutral atomic gas, in addition to the information on the dust discussed in this paper. The HI survey ALFALFA (Giovanelli et al. 2005, 2007) has given us the important opportunity to survey the HI content of Virgo galaxies in a complete and uniform way, as HeViCS is doing for the dust content. We published the first results on the HI content of Virgo ETG from ALFALFA in a previous paper (di Serego Alighieri et al. 2007, hereafter dSA07) in which we surveyed the 8–16 deg declination strip, for which the HI data were available at that time. Recently the ALFALFA survey has been extended to the 4–8 deg declination strip (Haynes et al. 2011, the so-called α.40), thereby covering the HeViCS area almost completely. Therefore we update here the list of HI-detected

ETG in the Virgo cluster for the 4–16 deg declination strip (see Table B.1). The criteria of this HI survey are the same as in dSA07, with the exception that we have now included the S0a-S0/SA galaxies (GOLDMine type = 2) among the surveyed ETG, in order to be consistent with what we have done for the HeViCS input ETG sample in the present paper. Actually, two such galaxies have been detected in HI, one of which is in the 8–16 declination strip, already surveyed by dSA07. There is another change from dSA07: we are now using the distances as reported in GOLDMine, which are different for the various cluster components (Gavazzi et al. 1999). This has an obvious effect, even on distance dependent parameters, such as the luminosity and the derived HI mass. The current α.40 catalogue only contains sources detected with code 1 or 2 (see Haynes et al. 2011). Therefore VCC 1964, which was detected with code 4 and was reported in dSA07, is not in the current list of HI detected ETG. The faint dE galaxy VCC 1202 deserves a special mention. We have remeasured its accurate position (see Appendix A), which is different from the position of the galaxy identified by Haynes et al. (2011) as the optical counterpart of the HI source AGC 223724, although the latter is identified as VCC 1202 in their catalogue. The position of the optical counterpart of AGC 223724 given by Haynes et al. (2011) corresponds to a 18 mag galaxy to the south-west, which is indeed the most likely HI counterpart. This galaxy is the faint blue galaxy No. 133 in Boerngen (1984), but does not correspond to VCC 1202 of Binggeli et al. (1985), which is the much fainter and smaller galaxy for which we give an accurate position in Table A.1. We have therefore excluded VCC 1202 from the list of Virgo ETG detected in HI.

In summary, 26 Virgo ETG are detected in HI, 22 of which are in the complete part of the optical sample ($m_{pg} \leq 18.0$), mostly based on the VCC. The sample of ETG examined in this update are all the galaxies present in GOLDMine, which have a GOLDMine type $-3 \leq T \leq 2$, which do not have a radial velocity $v_{hel} \geq 3000$ km s^{-1}, and which are in the 4–16 deg declination strip. There are 1164 such galaxies, 575 of which are in the complete optical sample. In order to examine the HI detection rate among Virgo ETG, we limit ourselves to this complete sample and we also take into account that ALFALFA has a much lower sensitivity in the region within one degree from M 87, since this is a strong radio continuum source. Therefore, if we exclude the 59 ETG of the complete sample which are included in this M 87 region, we have an HI detection rate for Virgo ETG brighter than $m_{pg} = 18.0$ of 22 galaxies out of 516, i.e. 4.3%. The fact that this rate is higher than the one obtained by dSA07 (2.3%) is only marginally influenced by the fact that we have now included S0a-S0/SA galaxies, and is most likely thanks to the higher HI detection rate in the outskirts of the Virgo cluster, as already remarked in dSA07, and has therefore been increased by the inclusion of the 4–8 deg declination strip, which covers these outskirts. However, the main conclusions of dSA07 and the conclusions drawn from the comparison with a sample of field ETG where the HI detection rate is much higher (Grossi et al. 2009), are still valid.

References

Auld, R., Bianchi, S., Smith, M. W. L., et al. 2013, MNRAS, 428, 1880
Baes, M., & Dejonghe, H. 2001, ApJ, 563, L19
Baes, M., & Dejonghe, H. 2002, MNRAS, 335, 441
Baes, M., Clemens, M., Xilouris, E. M., et al. 2010, A&A, 518, L53
Bertola, F., & Galletta, G. 1978, ApJ, 226, L115
Binggeli, B., Sandage, A., & Tammann, G. A. 1985, AJ, 90, 1681
Binggeli, B., Popescu, C. C., & Tammann, G. A. 1993, A&AS, 98, 275
Boerngen, F. 1984, Astron. Nachr., 305, 41
Boselli, A., Ciesla, L., Buat, V., et al. 2010a, A&A, 518, L61
Boselli, A., Eales, S., Cortese, L., et al. 2010b, PASP, 122, 261
Bruzual, G., & Charlot, S. 2003, MNRAS, 344, 1000
Buson, L., Bressan, A., Panuzzo, P., et al. 2009, ApJ, 705, 356
Cappellari, M., Emsellem, E., Krajnović, D., et al. 2011, MNRAS, 413, 813
Cardelli, J. A., Clayton, G. C., & Mathis, J. S. 1989, ApJ, 345, 245
Chabrier, G. 2003, ApJ, 586, L133
Ciesla, L., Boselli, A., Smith, M. W. L., et al. 2012, A&A, 543, A161
Clemens, M. S., Jones, A. P., Bressan, A., et al. 2010, A&A, 518, L50
Combes, F., Young, L. M., & Bureau, M. 2007, MNRAS, 377, 1795
Cortese, L., Davies, J. I., Pohlen, M., et al. 2010, A&A, 518, L49
Cortese, L., Ciesla, L., Boselli, A., et al. 2012, A&A, 540, A52
Dasyra, K. M., Combes, F., Salomé, P., & Braine, J. 2012, A&A, 540, A112
Davies, J. I., Baes, M., Bendo, G. J., et al. 2010, A&A, 518, L48
Davies, J. I., Bianchi, S., Cortese, L., et al. 2012, MNRAS, 419, 3505
Davis, T. A., Alatalo, K., Sarzi, M., et al. 2011, MNRAS, 417, 882
di Serego Alighieri, S., Gavazzi, G., Giovanardi, C., et al. 2007, A&A, 474, 851
Draine, B. T. 2003, ARA&A, 41, 241
Draine, B. T., Dale, D. A., Bendo, G., et al. 2007, ApJ, 663, 866
Ebneter, K., & Balick, B. 1985, AJ, 90, 183
Emsellem, E., Cappellari, M., Krajnović, D., et al. 2011, MNRAS, 414, 888
Ferrarese, L., Côté, P., Cuillandre, J.-C., et al. 2012, ApJS, 200, 4
Gavazzi, G., Boselli, A., Scodeggio, M., Pierini, D., & Belsole, E. 1999, MNRAS, 304, 595
Gavazzi, G., Boselli, A., Donati, A., Franzetti, P., & Scodeggio, M. 2003, A&A, 400, 451
Giovanelli, R., Haynes, M. P., Kent, B. R., et al. 2005, AJ, 130, 2613
Giovanelli, R., Haynes, M. P., Kent, B. R., et al. 2007, AJ, 133, 2569
Gomez, H. L., Baes, M., Cortese, L., et al. 2010, A&A, 518, L45
Goudfrooij, P., de Jong, T., Hansen, L., & Norgaard-Nielsen, H. U. 1994, MNRAS, 271, 833
Griffin, M. J., Abergel, A., Abreu, A., et al. 2010, A&A, 518, L3
Grossi, M., di Serego Alighieri, S., Giovanardi, C., et al. 2009, A&A, 498, 407
Haynes, M. P., Giovanelli, R., Martin, A. M., et al. 2011, AJ, 142, 170
Hollenbach, D., & Salpeter, E. E. 1971, ApJ, 163, 155
Kaviraj, S., Schawinski, K., Devriendt, J. E. G., et al. 2007, ApJS, 173, 619
Knapp, G. R., Guhathakurta, P., Kim, D.-W., & Jura, M. A. 1989, ApJS, 70, 329
Kuntschner, H., Emsellem, E., Bacon, R., et al. 2010, MNRAS, 408, 97
Leeuw, L. L., Sansom, A. E., Robson, E. I., Haas, M., & Kuno, N. 2004, ApJ, 612, 837
Lisker, T., Grebel, E. K., Binggeli, B., & Glatt, K. 2007, ApJ, 660, 1186
Magrini, L., Bianchi, S., Corbelli, E., et al. 2011, A&A, 535, A13
O'Donnell, J. E. 1994, ApJ, 422, 158
Ott, S. 2010, in Astronomical Data Analysis Software and Systems XIX, eds. Y. Mizumoto, K.-I. Morita, & M. Ohishi, ASP Conf. Ser., 434, 139
Perlman, E. S., Mason, R. E., Packham, C., et al. 2007, ApJ, 663, 808
Pierini, D., Maraston, C., Bender, R., & Witt, A. N. 2004, MNRAS, 347, 1
Poglitsch, A., Waelkens, C., Geis, N., et al. 2010, A&A, 518, L2
Roberts, M. S., Hogg, D. E., Bregman, J. N., Forman, W. R., & Jones, C. 1991, ApJS, 75, 751
Sandage, A., & Binggeli, B. 1984, AJ, 89, 919
Savoy, J., Welch, G. A., & Fich, M. 2009, ApJ, 706, 21
Schlegel, D. J., Finkbeiner, D. P., & Davis, M. 1998, ApJ, 500, 525
Smith, M. W. L., Vlahakis, C., Baes, M., et al. 2010, A&A, 518, L51
Smith, M. W. L., Gomez, H. L., Eales, S. A., et al. 2012, ApJ, 748, 123
Sparks, W. B., Ford, H. C., & Kinney, A. L. 1993, ApJ, 413, 531
Sparks, W. B., Pringle, J. E., Carswell, R. F., et al. 2012, ApJ, 750, L5
Taylor, E. N., Hopkins, A. M., Baldry, I. K., et al. 2011, MNRAS, 418, 1587
Taylor, R., Davies, J. I., Auld, R., & Minchin, R. F. 2012, MNRAS, 423, 787
Temi, P., Brighenti, F., Mathews, W. G., & Bregman, J. D. 2004, ApJS, 151, 237
Temi, P., Brighenti, F., & Mathews, W. G. 2007, ApJ, 660, 1215
Tody, D. 1993, in Astronomical Data Analysis Software and Systems II, eds. R. J. Hanisch, R. J. V. Brissenden, & J. Barnes, ASP Conf. Ser., 52, 173
Welch, G. A., Sage, L. J., & Young, L. M. 2010, ApJ, 725, 100
Witt, A. N., Thronson, Jr., H. A., & Capuano, Jr., J. M. 1992, ApJ, 393, 611
Xilouris, E. M., Madden, S. C., Galliano, F., Vigroux, L., & Sauvage, M. 2004, A&A, 416, 41
Young, L. M. 2002, AJ, 124, 788
Young, J. S., & Scoville, N. Z. 1991, ARA&A, 29, 581
Young, L. M., Bureau, M., Davis, T. A., et al. 2011, MNRAS, 414, 940
Zibetti, S., Charlot, S., & Rix, H.-W. 2009, MNRAS, 400, 1181

Pages 19 to 22 are available in the electronic edition of the journal at http://www.aanda.org

Table A.1. Revised coordinates.

VCC	RA (J2000)			Dec (J2000)			offset	m_{pg}	Type
	h	m	s	d	′	″	″		
2	12	8	25.31	13	49	42	1.3	18.5	–1
8	12	9	20.99	13	31	32	4.2	19.0	–1
11	12	9	35.60	6	44	35	4.5	17.0	–1
13	12	9	45.84	13	33	7	10.1	18.6	20
23	12	10	24.94	13	21	58	6.6	18.5	–1
35	12	11	19.48	11	54	36	6.3	19.0	20
42	12	12	5.99	14	57	11	10.0	19.5	–1
44	12	12	6.37	9	53	47	6.5	19.0	–1
55	12	12	26.81	13	16	46	3.5	18.7	–1
63	12	12	41.39	10	9	55	5.8	19.3	–1
69	12	12	55.57	10	33	35	4.3	18.5	–1
70	12	12	56.19	13	4	11	5.4	18.0	–1
80	12	13	23.65	7	45	9	8.3	20.0	–1
85	12	13	35.84	13	2	4	10.2	17.5	20
90	12	13	47.88	14	50	14	10.0	18.5	–1
91	12	13	47.56	6	21	46	11.4	18.0	–1
98	12	13	54.16	13	52	20	9.1	18.5	12
100	12	14	4.58	13	39	8	8.6	18.5	–1
104	12	14	8.87	9	43	15	6.2	18.0	19
112	12	14	29.56	14	4	36	5.4	19.5	–1
116	12	14	35.69	7	15	13	5.7	17.2	12
129	12	15	2.09	12	32	50	8.7	14.6	4
133	12	15	4.54	13	6	29	17.4	19.5	–1
136	12	15	6.59	4	47	45	7.4	18.5	20
139	12	15	12.32	11	0	1	4.1	19.3	–1
151	12	15	29.30	13	58	6	3.2	19.5	–1
156	12	15	35.77	11	44	39	2.2	19.5	–1
164	12	15	53.02	12	1	48	6.4	20.0	–1
171	12	16	12.04	8	22	24	195	17.4	12
185	12	16	19.63	13	8	9	8.3	19.3	–1
188	12	16	22.52	14	15	24	5.2	19.0	–1
190	12	16	22.95	7	47	55	8.2	18.0	–1
197	12	16	32.57	13	9	50	6.9	19.5	–1
204	12	16	39.02	12	52	20	4.1	18.5	20
205	12	16	42.50	6	41	21	6.2	19.3	–1
211	12	16	56.26	4	3	27	8.2	17.5	–1
214	12	16	57.69	4	51	27	5.0	18.2	–1
219	12	17	7.99	7	21	12	4.2	19.5	20
229	12	17	18.56	8	13	7	11.0	20.0	–1
232	12	17	24.68	13	30	39	25.0	19.0	–1
239	12	17	30.69	10	9	32	8.9	20.0	–1
240	12	17	31.26	14	21	21	1.4	19.3	–1
242	12	17	36.29	5	25	29	8.9	18.5	–1
244	12	17	39.73	5	20	29	3.6	18.0	–1
247	12	17	40.40	8	23	12	7.6	18.0	20
250	12	17	45.55	6	25	51	5.5	19.5	–1
252	12	17	46.00	5	26	53	3.1	17.3	–1
253	12	17	46.30	3	51	47	6.0	19.0	–1
254	12	17	46.05	6	25	24	5.5	20.0	–1
255	12	17	46.60	7	15	44	8.0	18.5	12
274	12	18	7.53	5	55	49	52.3	17.5	17
276	12	18	12.37	5	39	8	6.5	18.4	20
285	12	18	26.99	10	39	2	3.0	19.5	–1
290	12	18	30.58	12	23	57	7.7	20.0	–1
291	12	18	31.38	4	58	44	1.8	18.8	–1
294	12	18	35.26	6	29	39	6.9	18.0	–1
296	12	18	37.31	6	18	47	2.4	19.3	–1
306	12	18	48.35	8	59	17	9.6	19.3	–1
310	12	18	53.82	12	11	38	3.3	19.5	–1
316	12	19	1.19	5	46	23	63.2	19.3	20
317	12	19	2.70	5	5	51	8.9	18.0	–1
320	12	19	5.13	4	39	35	9.0	16.5	18
326	12	19	11.52	6	29	34	1.8	20.0	–1
360	12	19	36.86	15	27	17	15.2	18.5	–1
365	12	19	44.57	3	50	40	14.3	18.7	–1
367	12	19	45.30	5	27	21	9.1	17.2	12
368	12	19	44.86	7	37	49	12.0	19.0	–1
372	12	19	47.65	14	42	22	9.5	18.0	–1
379	12	19	51.64	5	59	46	11.1	17.0	20
381	12	19	53.59	6	39	56	7.7	16.5	12
383	12	19	57.24	9	33	32	6.7	20.0	–1
384	12	19	58.60	6	20	3	8.3	20.0	–1
387	12	20	3.57	5	43	13	7.9	18.5	–1
399	12	20	14.20	5	54	56	0.3	19.0	–1
403	12	20	17.55	10	19	15	9.3	18.0	–1
405	12	20	17.87	6	0	6	10.6	20.0	–1
412	12	20	24.51	10	40	53	14.8	20.0	–1
414	12	20	24.37	14	41	28	10.9	17.9	19
416	12	20	26.83	12	47	50	14.6	20.0	19
418	12	20	26.86	14	47	7	8.2	17.9	–1
425	12	20	35.73	8	12	4	4.9	17.3	12
427	12	20	41.20	4	47	49	10.5	18.5	–1
431	12	20	46.37	12	45	27	7.8	18.5	–1
440	12	20	52.21	5	13	55	6.3	17.2	–1
441	12	20	52.85	6	19	28	12.5	18.5	20
444	12	20	54.68	14	59	22	11.7	17.2	–1
456	12	21	9.06	12	17	58	8.2	19.5	–1
457	12	21	9.88	6	22	8	7.6	19.0	–1
467	12	21	19.27	3	47	16	5.0	17.7	12
476	12	21	29.11	10	29	10	10.9	17.9	12
477	12	21	27.10	15	1	12	20.1	17.0	12
480	12	21	29.24	12	47	52	8.2	19.5	–1
481	12	21	30.81	15	30	3	9.1	18.3	–1
484	12	21	33.94	6	32	49	17.4	19.2	–1
496	12	21	42.73	9	21	19	5.2	18.7	–1
499	12	21	44.56	9	14	12	12.8	17.6	–1
502	12	21	48.83	11	51	6	7.6	19.5	–1
506	12	21	54.53	4	45	12	14.2	18.5	–1
507	12	21	52.30	15	22	56	8.0	19.0	–1
511	12	21	55.83	8	20	45	9.6	18.2	–1
518	12	22	0.21	11	38	8	7.2	20.0	20
532	12	22	10.46	11	38	29	7.8	18.7	–1
537	12	22	12.78	12	41	48	10.4	18.5	–1
540	12	22	16.90	10	57	12	3.1	19.4	–1
548	12	22	22.90	3	44	39	7.2	18.3	12
555	12	22	27.55	7	5	52	0.8	19.2	–1
563	12	22	35.27	16	20	52	6.1	16.3	–1
564	12	22	36.50	11	17	50	17.1	20.0	–1
569	12	22	39.05	10	37	43	9.4	19.5	–1
577	12	22	44.62	5	24	55	9.0	18.3	–1
579	12	22	45.33	7	15	51	2.6	20.0	–1
581	12	22	46.55	7	6	4	3.8	20.0	20
582	12	22	47.24	8	26	14	10.2	20.0	–1
585	12	22	46.97	11	20	40	18.9	17.0	12
589	12	22	51.18	7	4	13	4.7	19.8	–1
590	12	22	51.04	8	54	8	6.0	19.0	–1
591	12	22	51.85	7	7	59	5.7	20.0	–1
595	12	22	53.72	12	23	19	9.2	19.5	–1
609	12	23	3.46	8	32	7	8.7	19.2	20
610	12	23	3.17	16	19	41	4.7	20.0	–1
612	12	23	5.32	4	7	48	6.7	17.3	20
614	12	23	4.17	14	48	21	14.6	18.6	–1
628	12	23	16.15	7	41	13	12.7	18.2	12
629	12	23	17.67	6	54	43	6.0	18.2	12
631	12	23	18.46	7	39	46	5.1	18.5	–1
633	12	23	21.43	7	35	30	8.6	18.0	–1
639	12	23	25.19	6	59	54	3.7	19.0	–1
642	12	23	30.33	5	29	41	5.4	18.3	–1
645	12	23	31.88	11	16	14	8.0	18.2	–1
653	12	23	36.91	7	35	44	6.8	17.6	–1
658	12	23	39.33	10	1	51	2.6	18.5	–1
659	12	23	38.54	12	37	39	5.3	18.3	–1

Table A.1. continued.

VCC	RA (J2000)			Dec (J2000)			offset	m_{pg}	Type
	h	m	s	d	′	″	″		
661	12	23	41.31	7	17	27	7.9	18.5	–1
666	12	23	46.24	16	47	26	2.1	16.8	12
671	12	23	52.81	5	45	19	3.5	18.0	–1
676	12	23	54.20	6	54	2	5.1	19.5	–1
678	12	23	52.94	12	46	22	22.1	18.3	–1
686	12	23	59.83	9	29	37	4.7	18.5	–1
689	12	23	59.92	17	39	5	5.8	19.8	20
691	12	24	0.63	11	51	34	8.4	19.5	–1
694	12	24	5.80	7	31	53	7.4	18.8	–1
701	12	24	8.25	11	8	45	4.8	19.2	–1
702	12	24	9.05	8	30	49	4.5	19.5	–1
705	12	24	10.94	11	56	47	14.1	17.2	–1
707	12	24	12.92	11	45	41	2.7	19.0	–1
709	12	24	12.73	14	29	36	67.5	19.0	–1
716	12	24	13.68	14	55	44	13.8	19.2	–1
724	12	24	25.63	7	7	51	1.4	18.3	–1
730	12	24	27.99	6	40	36	16.0	20.0	–1
732	12	24	30.96	11	48	41	12.0	18.5	–1
743	12	24	42.50	11	28	56	13.5	20.0	–1
744	12	24	46.84	7	55	3	8.0	19.0	–1
746	12	24	47.67	8	26	19	2.8	17.7	–1
752	12	24	47.90	11	49	6	31.3	19.0	–1
769	12	25	4.23	15	42	40	17.8	17.2	–1
774	12	25	10.05	10	27	23	7.3	18.5	–1
776	12	25	11.15	6	18	51	25.5	18.2	–1
783	12	25	15.57	7	14	18	8.0	19.0	–1
791	12	25	22.21	6	42	40	7.3	16.4	–1
803	12	25	28.97	12	29	37	12.7	18.0	–1
807	12	25	33.18	7	48	28	7.6	19.0	–1
811	12	25	38.23	10	15	0	31.7	16.5	19
814	12	25	36.67	12	50	59	3.3	19.0	20
824	12	25	38.70	14	9	2	11.5	18.0	–1
842	12	25	48.55	12	13	32	7.0	20.0	–1
853	12	25	55.75	11	48	4	28.1	20.0	–1
875	12	26	9.87	7	18	8	7.4	19.8	20
879	12	26	12.30	6	5	10	6.4	19.0	–1
880	12	26	12.13	12	5	10	6.4	19.6	–1
883	12	26	15.47	7	45	21	7.2	19.0	–1
884	12	26	15.34	13	8	35	5.9	18.5	–1
886	12	26	15.29	13	20	26	8.2	20.0	–1
895	12	26	24.92	10	34	53	33.5	18.3	–1
896	12	26	22.58	12	47	9	10.0	18.0	–1
900	12	26	25.99	13	44	18	9.9	18.5	–1
901	12	26	26.12	16	31	23	1.2	18.0	–1
902	12	26	28.65	8	47	43	13.4	19.1	–1
903	12	26	28.07	12	55	13	13.4	18.9	–1
906	12	26	29.85	9	58	44	20.9	19.0	–1
914	12	26	34.28	8	59	34	7.3	19.0	–1
922	12	26	36.98	10	12	28	25.5	18.2	–1
923	12	26	36.36	12	48	10	4.5	19.5	–1
924	12	26	34.90	13	52	13	18.0	19.3	–1
925	12	26	38.06	15	5	7	17.2	19.5	–1
930	12	26	41.11	12	50	43	11.5	18.0	–1
937	12	26	46.58	13	15	59	13.1	19.0	–1
943	12	26	47.58	13	40	47	9.6	18.6	–1
948	12	26	53.28	7	45	9	6.9	20.0	–1
954	12	26	56.31	5	58	18	12.3	17.2	–1
960	12	26	58.80	6	48	3	6.6	20.0	–1
964	12	27	1.91	14	6	31	8.7	18.4	–1
967	12	27	3.81	12	51	58	4.7	18.7	–1
968	12	27	6.04	13	19	24	5.7	19.2	–1
970	12	27	7.97	7	48	59	12.3	19.5	–1
982	12	27	12.73	17	49	15	2.5	17.3	–1
983	12	27	15.16	9	37	34	24.7	18.0	–1
988	12	27	17.67	6	46	2	7.3	20.0	–1
993	12	27	20.55	9	35	29	22.6	18.5	–1

Table A.1. continued.

VCC	RA (J2000)			Dec (J2000)			offset	m_{pg}	Type
	h	m	s	d	′	″	″		
999	12	27	24.11	12	7	59	12.8	19.7	–1
1000	12	27	24.73	11	14	17	8.0	18.2	–1
1004	12	27	24.90	13	24	23	15.6	19.0	–1
1006	12	27	25.24	14	26	1	10.9	18.2	–1
1009	12	27	27.03	8	21	8	11.6	19.5	–1
1012	12	27	28.46	8	23	28	17.4	20.0	–1
1014	12	27	29.77	12	15	5	1.0	18.3	–1
1023	12	27	34.38	12	48	13	12.0	20.0	–1
1027	12	27	39.23	12	52	47	18.0	18.1	–1
1029	12	27	39.02	14	32	31	8.7	19.0	–1
1032	12	27	42.65	6	22	6	2.2	19.5	12
1038	12	27	41.82	14	35	55	11.7	18.6	20
1040	12	27	44.53	12	59	1	6.5	17.5	–1
1041	12	27	46.50	11	44	28	12.1	19.5	20
1045	12	27	49.64	7	1	33	17.0	18.7	12
1046	12	27	49.43	12	29	59	10.2	20.0	–1
1050	12	27	55.16	8	50	53	2.7	18.5	–1
1051	12	27	54.55	12	36	15	4.5	19.8	–1
1053	12	27	54.79	13	49	15	10.1	19.5	–1
1054	12	27	56.02	8	5	15	9.5	18.5	–1
1056	12	27	57.33	14	28	13	2.6	18.7	–1
1067	12	28	6.31	8	3	42	7.3	20.0	20
1070	12	28	6.73	12	58	43	11.3	19.6	–1
1071	12	28	7.21	8	48	54	5.9	18.4	–1
1077	12	28	10.24	12	48	31	7.1	19.2	–1
1081	12	28	12.85	13	0	54	10.9	18.8	–1
1082	12	28	14.32	6	18	40	9.7	20.0	20
1089	12	28	17.65	10	52	6	15.5	17.9	–1
1090	12	28	17.84	9	43	40	7.1	19.0	–1
1092	12	28	20.08	9	10	12	6.2	17.0	–1
1094	12	28	20.68	6	11	43	3.4	17.3	20
1097	12	28	20.25	15	41	59	8.2	19.0	–1
1098	12	28	22.39	8	43	41	4.6	18.5	12
1106	12	28	31.47	10	31	7	32.5	17.5	12
1108	12	28	29.78	8	32	16	5.8	19.5	–1
1109	12	28	31.09	6	54	16	8.3	18.5	–1
1112	12	28	31.46	16	3	51	2.7	18.8	–1
1113	12	28	34.03	7	34	17	4.5	19.5	–1
1115	12	28	32.42	11	44	39	13.0	17.7	–1
1117	12	28	40.00	8	49	37	4.5	19.0	–1
1121	12	28	41.08	11	7	57	10.9	16.5	12
1124	12	28	44.10	10	51	56	20.5	16.3	–1
1128	12	28	44.95	9	3	15	4.5	17.3	12
1133	12	28	48.47	8	13	53	5.3	19.3	–1
1137	12	28	49.68	14	9	26	17.9	17.2	–1
1140	12	28	52.63	14	23	38	9.8	18.5	–1
1151	12	28	59.22	7	31	35	7.3	16.7	–1
1159	12	29	4.28	4	50	55	9.3	19.0	–1
1160	12	29	4.25	8	27	21	10.3	18.3	12
1165	12	29	10.28	9	16	0	1.4	17.9	19
1167	12	29	14.69	7	52	39	37.2	15.9	–1
1170	12	29	13.03	10	59	26	7.2	19.0	–1
1171	12	29	14.60	8	14	29	9.2	19.2	–1
1176	12	29	18.96	8	1	11	6.8	19.0	20
1180	12	29	21.20	16	48	22	8.7	16.5	–1
1194	12	29	29.29	14	10	10	9.2	18.3	–1
1195	12	29	31.91	7	49	18	6.4	19.0	19
1201	12	29	34.51	13	19	56	13.7	18.8	–1
1202	12	29	35.58	13	12	39	8.8	20.0	–1
1207	12	29	37.95	9	31	15	3.3	17.5	–1
1211	12	29	39.64	9	27	48	5.9	18.2	–1
1212	12	29	39.02	11	38	0	10.6	16.9	–1
1214	12	29	38.41	14	3	30	16.6	20.0	–1
1215	12	29	40.45	16	57	42	8.5	19.4	–1
1220	12	29	42.96	14	22	4	9.5	19.0	20
1221	12	29	43.41	17	30	55	4.4	18.2	–1

Table A.1. continued.

VCC	RA (J2000)			Dec (J2000)			offset	m_{pg}	Type
	h	m	s	d	′	″	″		
1227	12	29	46.98	11	10	12	18.3	17.9	19
1228	12	29	45.12	14	37	52	13.2	16.2	–1
1229	12	29	47.15	13	4	34	5.2	19.4	20
1230	12	29	49.50	7	17	1	5.1	19.5	12
1232	12	29	49.30	11	29	36	4.6	19.0	20
1236	12	29	51.98	6	11	39	4.7	18.4	–1
1244	12	29	56.35	13	13	12	9.2	18.9	–1
1246	12	29	59.40	10	51	21	25.9	18.2	–1
1248	12	29	57.64	14	28	21	5.5	18.2	–1
1251	12	30	1.13	13	7	4	11.8	19.8	–1
1255	12	30	6.85	6	20	36	12.2	19.0	12
1265	12	30	11.56	13	41	28	16.2	19.0	–1
1267	12	30	13.34	7	6	9	5.3	19.3	–1
1275	12	30	17.73	7	53	2	8.8	20.0	–1
1276	12	30	18.14	14	40	51	22.2	20.0	–1
1280	12	30	17.20	14	7	45	9.6	19.5	20
1281	12	30	18.78	7	54	19	9.2	19.5	–1
1282	12	30	18.21	12	34	17	58.1	19.7	–1
1285	12	30	20.31	14	8	24	15.9	18.5	–1
1296	12	30	32.71	6	31	56	1.3	17.2	–1
1301	12	30	38.22	13	37	10	8.6	19.0	–1
1306	12	30	45.88	9	0	42	4.3	19.5	–1
1310	12	30	46.88	13	12	49	6.4	19.3	–1
1312	12	30	47.27	11	32	15	29.0	18.7	–1
1319	12	30	52.31	13	51	30	4.7	19.5	–1
1325	12	30	56.01	13	26	55	4.2	20.0	–1
1328	12	30	57.37	13	37	12	9.3	19.3	–1
1329	12	31	0.56	5	33	18	12.4	18.1	–1
1332	12	31	2.32	6	7	20	12.3	18.3	19
1336	12	31	3.96	11	50	11	6.2	17.0	19
1337	12	31	4.84	15	4	12	15.0	18.0	–1
1338	12	31	4.64	17	23	16	9.5	18.7	–1
1342	12	31	13.79	6	40	16	4.9	19.0	–1
1344	12	31	14.22	16	57	4	8.1	20.0	–1
1345	12	31	15.83	9	21	32	7.4	19.0	–1
1349	12	31	17.32	7	51	40	4.3	18.5	–1
1357	12	31	24.42	9	28	28	4.0	18.9	12
1361	12	31	27.13	9	43	59	6.2	17.2	–1
1364	12	31	28.86	3	58	28	12.5	19.5	–1
1365	12	31	30.73	10	0	19	5.2	19.3	–1
1367	12	31	33.10	8	58	4	28.4	19.5	12
1370	12	31	36.88	11	0	26	31.6	17.4	–1
1371	12	31	35.79	13	49	27	6.6	18.2	–1
1372	12	31	35.87	16	43	29	8.9	19.5	–1
1378	12	31	41.67	5	46	27	9.0	18.2	–1
1382	12	31	44.58	10	0	46	3.7	19.5	20
1383	12	31	46.63	9	5	1	12.5	18.5	20
1384	12	31	46.63	10	40	27	19.8	17.1	–1
1387	12	31	50.53	13	40	50	12.7	19.2	–1
1388	12	31	49.91	16	58	18	4.9	19.0	12
1390	12	31	51.83	14	22	20	12.6	20.0	–1
1391	12	31	53.82	5	10	22	2.2	18.5	–1
1397	12	31	59.98	3	32	24	6.9	18.0	12
1403	12	32	0.25	13	4	52	7.9	17.1	12
1404	12	32	1.51	8	40	10	6.2	18.1	–1
1406	12	32	2.77	8	4	30	4.9	19.6	–1
1408	12	32	4.41	7	56	37	2.0	18.0	19
1415	12	32	8.81	8	2	21	4.3	19.5	–1
1421	12	32	13.00	9	18	54	2.8	20.0	–1
1424	12	32	20.56	10	18	37	8.4	19.5	20
1425	12	32	20.78	10	3	26	5.8	18.9	–1
1433	12	32	28.46	14	21	45	13.7	19.0	–1
1434	12	32	29.82	14	39	44	36.9	20.0	–1
1439	12	32	35.23	8	38	10	6.6	20.0	–1
1447	12	32	38.66	10	45	34	15.9	19.5	–1
1467	12	32	55.00	13	53	19	7.4	18.8	–1

Table A.1. continued.

VCC	RA (J2000)			Dec (J2000)			offset	m_{pg}	Type
	h	m	s	d	′	″	″		
1470	12	33	0.40	10	7	42	3.4	20.0	–1
1477	12	33	6.41	13	18	10	11.3	19.0	–1
1478	12	33	6.22	15	30	27	7.5	18.3	–1
1487	12	33	12.28	8	22	39	8.2	19.5	–1
1505	12	33	24.64	15	24	27	10.6	18.0	–1
1506	12	33	27.96	7	51	16	5.4	18.3	–1
1510	12	33	30.14	16	17	43	5.0	18.3	12
1511	12	33	33.21	13	28	36	9.9	18.2	–1
1515	12	33	41.11	3	40	33	3.2	17.0	20
1520	12	33	42.25	10	47	14	6.8	20.0	–1
1527	12	33	50.52	10	59	14	9.9	19.8	–1
1533	12	34	1.47	5	57	11	1.5	18.0	–1
1534	12	34	1.60	6	38	42	4.9	18.2	–1
1543	12	34	9.67	16	42	42	4.0	18.0	–1
1546	12	34	11.28	13	34	22	6.9	19.5	–1
1547	12	34	14.87	2	17	47	1.5	18.2	–1
1553	12	34	16.13	16	3	31	14.8	16.7	–1
1556	12	34	18.61	14	28	23	10.2	19.3	–1
1560	12	34	23.04	10	57	48	10.6	20.0	20
1580	12	34	43.47	8	5	26	5.1	18.8	–1
1586	12	34	46.51	14	17	32	6.1	19.3	–1
1589	12	34	53.49	8	9	36	6.2	19.0	–1
1590	12	34	54.96	14	39	0	3.6	20.0	–1
1591	12	34	57.15	10	3	46	9.7	18.5	–1
1600	12	35	6.96	10	30	35	7.1	19.0	–1
1601	12	35	8.11	12	57	56	12.5	18.0	–1
1612	12	35	24.41	13	45	56	5.0	18.5	–1
1618	12	35	31.68	7	1	33	9.5	18.3	–1
1622	12	35	31.40	16	2	53	15.2	17.9	–1
1640	12	35	49.68	9	20	31	9.5	19.0	–1
1645	12	35	55.23	2	29	10	4.2	18.0	–1
1646	12	35	57.41	5	47	23	9.0	19.5	–1
1648	12	36	2.51	6	24	28	6.9	20.0	–1
1650	12	36	2.96	13	29	8	7.4	17.4	–1
1651	12	36	7.19	6	3	15	4.9	17.0	–1
1652	12	36	8.56	7	35	46	12.9	17.3	–1
1655	12	36	14.18	9	28	18	5.1	18.6	–1
1666	12	36	29.40	8	30	44	3.7	19.5	–1
1693	12	36	52.54	13	17	0	17.4	19.2	–1
1694	12	36	52.60	13	46	3	4.1	19.3	–1
1702	12	37	6.96	13	58	54	10.8	17.7	–1
1703	12	37	9.23	8	23	31	3.1	19.0	20
1705	12	37	10.84	9	29	24	9.1	17.8	–1
1707	12	37	15.11	10	43	13	2.0	19.0	–1
1714	12	37	25.24	14	18	44	7.8	18.5	–1
1716	12	37	27.09	15	8	56	6.3	19.0	–1
1719	12	37	31.17	9	30	20	6.4	18.5	–1
1723	12	37	36.29	9	12	24	1.4	20.0	–1
1724	12	37	41.08	7	40	37	5.9	18.5	–1
1731	12	37	49.11	13	26	24	5.5	18.5	–1
1732	12	37	50.26	15	43	38	14.0	17.8	–1
1733	12	37	52.17	14	28	1	12.5	18.0	–1
1734	12	37	54.04	2	8	56	6.1	20.0	–1
1735	12	37	52.62	2	10	50	25.6	19.5	–1
1738	12	37	54.74	15	9	32	1.8	18.3	–1
1739	12	37	57.71	6	32	31	10.6	18.7	–1
1741	12	38	2.77	2	22	10	8.4	18.4	–1
1742	12	38	4.00	9	31	26	4.5	19.0	–1
1749	12	38	12.13	10	42	7	8.2	19.5	–1
1751	12	38	13.56	15	22	25	2.4	18.6	–1
1753	12	38	16.01	14	52	12	1.9	16.8	12
1766	12	38	37.46	13	30	28	14.2	18.5	–1
1770	12	38	42.68	6	40	7	10.5	18.4	20
1771	12	38	43.88	9	31	56	1.3	18.0	12
1775	12	38	53.09	12	59	0	6.7	20.0	–1
1776	12	38	54.09	10	14	34	16.6	17.1	19

Table A.1. continued.

VCC	RA (J2000)			Dec (J2000)			offset	m_{pg}	Type
	h	m	s	d	′	″	″		
1784	12	39	14.18	15	37	38	12.8	15.8	12
1786	12	39	16.31	12	58	15	14.9	18.1	–1
1788	12	39	18.54	10	49	9	6.8	19.7	–1
1792	12	39	25.98	12	55	41	4.4	18.3	–1
1797	12	39	33.67	2	42	40	4.3	18.3	–1
1801	12	39	39.63	2	13	58	5.2	19.5	–1
1805	12	39	42.69	9	18	34	9.3	19.5	–1
1819	12	40	5.17	5	45	32	6.6	18.8	20
1820	12	40	4.17	13	2	3	9.2	19.0	12
1840	12	40	26.93	10	7	41	2.6	18.5	–1
1844	12	40	29.20	9	43	22	3.9	19.5	20
1850	12	40	34.13	15	22	2	12.8	19.5	20
1851	12	40	43.60	10	24	28	10.1	18.8	–1
1852	12	40	43.69	13	47	22	3.0	19.5	–1
1856	12	40	50.98	7	55	49	4.3	18.8	–1
1864	12	41	6.88	3	36	38	4.8	16.8	20
1867	12	41	10.66	15	2	55	20.8	17.7	–1
1872	12	41	19.04	2	6	0	16.0	18.5	–1
1874	12	41	18.12	13	9	54	15.4	17.7	–1
1877	12	41	23.95	8	21	56	3.7	18.6	–1
1884	12	41	39.36	9	12	33	19.5	16.7	19
1885	12	41	38.39	15	49	12	23.3	16.4	12
1899	12	41	57.45	8	49	52	7.7	20.0	–1
1900	12	41	57.24	13	4	5	13.6	16.6	19
1907	12	42	5.99	4	12	18	12.1	19.0	20
1911	12	42	9.74	4	41	30	16.0	19.5	–1
1914	12	42	11.36	14	49	2	27.5	19.5	20
1919	12	42	18.21	10	34	3	10.2	17.0	–1
1926	12	42	34.03	10	20	36	16.1	19.3	–1
1928	12	42	37.83	13	36	23	6.4	17.5	–1
1930	12	42	41.50	7	50	37	12.4	19.5	–1
1970	12	43	29.04	10	5	35	2.4	15.8	12
1974	12	43	37.05	3	21	45	15.5	19.0	–1
1975	12	43	35.42	10	45	20	11.9	18.8	–1
1976	12	43	35.81	13	15	2	4.4	18.5	–1
1994	12	44	13.19	9	43	23	6.1	16.8	19
1996	12	44	20.89	8	24	13	3.8	18.5	–1
2013	12	45	8.49	8	35	22	1.8	18.3	–1
2014	12	45	9.71	10	37	49	8.8	17.5	–1
2015	12	45	11.96	10	19	28	5.5	16.2	17
2021	12	45	27.71	13	1	36	7.5	19.0	–1
2022	12	45	33.11	8	43	45	4.0	20.0	–1
2026	12	45	34.66	14	23	13	0.9	20.0	–1
2027	12	45	36.91	10	35	56	15.3	18.5	12
2030	12	45	50.72	8	18	22	4.8	18.8	–1
2031	12	45	49.63	14	31	17	1.4	19.5	–1
2035	12	46	9.44	8	42	28	3.6	20.0	–1
2052	12	47	29.46	13	38	56	6.4	20.0	–1
2053	12	47	31.35	7	56	3	1.5	19.2	–1
2059	12	47	48.43	7	42	22	9.3	20.0	–1
2060	12	47	55.50	9	9	32	10.5	18.6	–1
2063	12	48	3.23	13	43	27	8.1	17.0	–1
2067	12	48	20.87	8	2	28	10.9	18.2	–1
2068	12	48	20.51	10	1	39	10.3	18.8	–1
2075	12	48	29.39	13	48	18	6.4	19.3	–1
2084	12	50	24.00	10	29	25	8.9	19.5	–1
2091	12	52	5.91	11	1	56	6.1	18.5	–1
2094	12	52	35.64	10	26	58	10.2	17.8	12